Cell Reports

Article

Early invasion of the bladder wall by solitary bacteria protects UPEC from antibiotics and neutrophil swarms in an organoid model

Graphical abstract

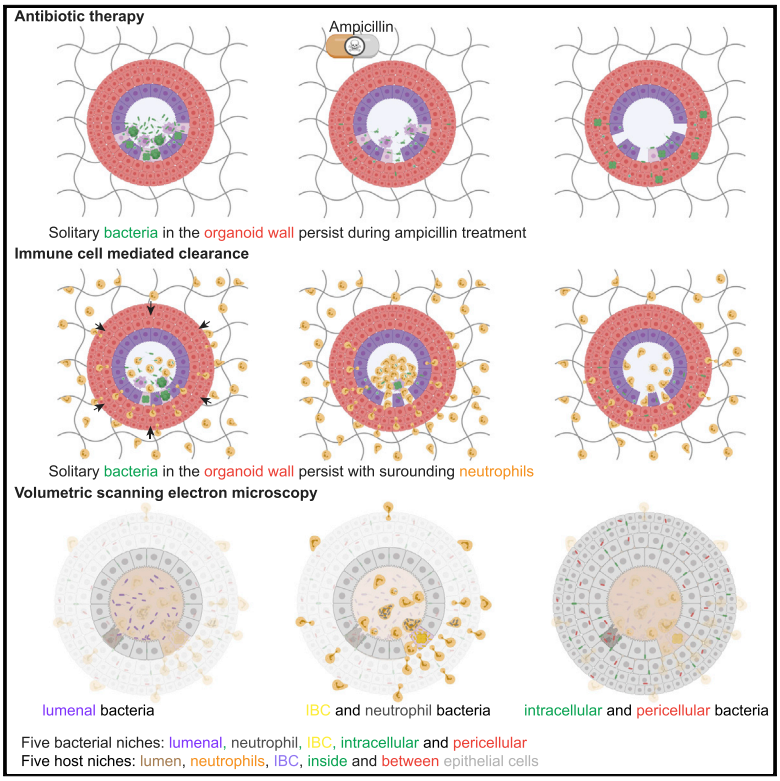

Highlights

- A bladder organoid model reproduces key features of urinary tract infections (UTIs)
- UPEC forms intracellular bacterial communities (IBCs) in bladder organoids
- QIR-like bacteria appear concurrently with and independently of IBCs
- QIR-like bacteria are protected from clearance by antibiotics and host immune cells

Authors

Kunal Sharma, Vivek V. Thacker, Neeraj Dhar, ..., Graham W. Knott, Hans Clevers, John D. McKinney

Correspondence

vivekvthacker@gmail.com (V.V.T.), neeraj.dhar@epfl.ch (N.D.), john.mckinney@epfl.ch (J.D.M.)

In brief

Sharma et al. present a bladder organoid model for uropathogenic *Escherichia coli* infections. High-resolution volumetric electron microscopy and time-lapse optical microscopy reveal that solitary bacteria rapidly invade deeper layers of the bladder epithelium, where they localize within or between uroepithelial cells and resist clearance by antibiotics or host immune cells.

Sharma et al., 2021, Cell Reports *36*, 109351
July 20, 2021 © 2021 The Authors.
https://doi.org/10.1016/j.celrep.2021.109351

CellPress

Cell Reports

CellPress
OPEN ACCESS

Article

Early invasion of the bladder wall by solitary bacteria protects UPEC from antibiotics and neutrophil swarms in an organoid model

Kunal Sharma,[1] Vivek V. Thacker,[1,3,*] Neeraj Dhar,[1,3,*] Maria Clapés Cabrer,[1] Anaëlle Dubois,[1] François Signorino-Gelo,[1] Jasper Mullenders,[2] Graham W. Knott,[1] Hans Clevers,[2] and John D. McKinney[1,4,*]
[1]School of Life Sciences, Swiss Federal Institute of Technology in Lausanne (EPFL), 1015 Lausanne, Switzerland
[2]Oncode Institute, Hubrecht Institute, Royal Netherlands Academy of Arts and Sciences and University Medical Center, Utrecht, the Netherlands
[3]These authors contributed equally
[4]Lead contact
*Correspondence: vivekvthacker@gmail.com (V.V.T.), neeraj.dhar@epfl.ch (N.D.), john.mckinney@epfl.ch (J.D.M.)
https://doi.org/10.1016/j.celrep.2021.109351

SUMMARY

Recurrence of uropathogenic *Escherichia coli* (UPEC) infections has been attributed to reactivation of quiescent intracellular reservoirs (QIRs) in deep layers of the bladder wall. QIRs are thought to arise late during infection following dispersal of bacteria from intracellular bacterial communities (IBCs) in superficial umbrella cells. Here, we track the formation of QIR-like bacteria in a bladder organoid model that recapitulates the stratified uroepithelium within a volume suitable for high-resolution live-cell imaging. Bacteria injected into the organoid lumen enter umbrella-like cells and proliferate to form IBC-like bodies. In parallel, single bacteria penetrate deeper layers of the organoid wall, where they localize within or between uroepithelial cells. These "solitary" bacteria evade killing by antibiotics and neutrophils and are morphologically distinct from bacteria in IBCs. We conclude that bacteria with QIR-like properties may arise at early stages of infection, independent of IBC formation and rupture.

INTRODUCTION

Urinary tract infections (UTIs) are among the most common bacterial infections and the second most common cause for the prescription of antibiotics (Foxman, 2010). Recurrence, defined as a reappearance of three or more episodes of infection within 12 months of apparently successful antibiotic therapy, occurs in a quarter of all UTIs (Epp et al., 2010; Foxman et al., 2000), and women are at particularly high risk (Klein and Hultgren, 2020). Uropathogenic *Escherichia coli* (UPEC) is the causative agent of about 80% of UTIs, which can be further complicated by dissemination of UPEC from the bladder to the kidneys or into the bloodstream.

Much of our current understanding of UPEC pathogenesis derives from mouse models of infection (Hannan and Hunstad, 2016; Hung et al., 2009), which reveal that UPEC can grow extracellularly in the urine (Alteri et al., 2009; Forsyth et al., 2018; Hull and Hull, 1997; Subashchandrabose et al., 2014) or intracellularly in the bladder wall (Anderson et al., 2003; Justice et al., 2004; Mulvey et al., 2001). Invasion of the bladder wall is mediated by interactions of the bacterial type I pilus with uroplakin proteins expressed on the superficial umbrella cell layer (Klein and Hultgren, 2020; Lewis et al., 2016; Martinez et al., 2000; Mulvey et al., 1998). Within umbrella cells, a subset of bacteria proliferate to form biofilm-like intracellular bacterial communities (IBCs) (Anderson et al., 2003; Justice et al., 2004; Mulvey et al., 2000) that protect the bacteria from clearance by antibiotics (Blango and Mulvey, 2010) or innate immunity (Justice et al., 2004). At later stages of infection, UPEC penetrates into deeper layers of the bladder to form quiescent intracellular reservoirs (QIRs) that may also be responsible for recurrent infection after antibiotic therapy (Mulvey et al., 2000, 2001; Mysorekar and Hultgren, 2006; Schilling et al., 2002).

The bacterial numbers in three identifiable subpopulations (extracellular bacteria, IBCs, and QIRs), their relative growth dynamics, and their survival under attack from antibiotics or immune cells are difficult to characterize *in situ* in animal models. Many studies have therefore relied on an examination of bladder explants at successive time points post-infection (Blango et al., 2014; Mulvey et al., 2001; Scott et al., 2015). Although powerful, this technique does not provide information on the underlying dynamics of host-pathogen interactions, nor does it permit the quantification of *in situ* growth of extracellular bacteria (Anderson et al., 2003; Justice et al., 2004). *In vitro* models have been developed to study specific aspects of UPEC infection, such as the role of the stratified bladder architecture (Horsley et al., 2018) or the effects of micturition on IBC formation (Andersen et al., 2012). However, these models suffer from limitations in their ability to recreate a stratified uroepithelium with multiple differentiated cell layers (Andersen et al., 2012), and three-dimensional (3D) migration of immune cells into the bladder in response to infection is difficult to model in platforms based on

This is an open access article under the CC BY-NC-ND license (http://creativecommons.org/licenses/by-nc-nd/4.0/).

Transwell inserts (Horsley et al., 2018). In many *in vitro* systems, live-cell imaging remains technically challenging (Horsley et al., 2018; Smith et al., 2006).

In the last decade, organoids have emerged as experimentally tractable biomimetic systems that recapitulate key physiological and functional features of the cognate organs (Clevers, 2016). These complex 3D multicellular structures are generated from stem cells or organ-specific progenitor cells (Rossi et al., 2018) and have now been established for a number of different organs (Liu et al., 2004; Sachs et al., 2019), including the bladder (Lee et al., 2018; Mullenders et al., 2019; Santos et al., 2019). Recently, organoids have also emerged as model systems to study host-pathogen interactions during infections caused by bacteria (Bartfeld and Clevers, 2015; Co et al., 2019; Kessler et al., 2019; Pleguezuelos-Manzano et al., 2020; Williamson et al., 2018), viruses (Qian et al., 2017; van der Sanden et al., 2018; Zhou et al., 2018), or parasites (Heo et al., 2018; Nikolaev et al., 2020).

Bladder organoids offer several distinct advantages as model systems for UTIs. They recapitulate the stratified and differentiated layers of the uroepithelium, possess a central lumen that mimics the bladder lumen, and are easier to manipulate than animal infection models. Importantly, the compact volume of an organoid can be imaged in its entirety with high spatiotemporal resolution using time-lapse confocal microscopy. This makes it possible to follow the rapidly changing dynamics of UTIs and to monitor the responses of host cells and bacteria to external perturbations, such as antibiotic treatment or the addition of innate immune cells (Neal et al., 2018; Sachs et al., 2019). Compared to *in vitro* infection models (Andersen et al., 2012), bladder organoids offer a more realistic reconstitution of bladder physiology that is accessible to a wider range of experimental techniques for studies of UPEC pathogenesis than conventional *ex vivo* tissue explants (Justice et al., 2004)

Here, we establish a model system to study the early dynamics of UPEC pathogenesis based on mouse bladder organoids derived from primary cells (Mullenders et al., 2019). We use a combination of time-lapse laser scanning confocal microscopy and serial block face scanning electron microscopy (SBEM) to monitor the dynamics of UPEC invasion, growth, and persistence within bladder organoids with single-cell and sub-micron resolution. We find that individual solitary bacteria are seeded in deeper layers of the bladder epithelium concomitantly with but independently of the formation of IBCs in the superficial layer of umbrella-like cells. These solitary bacteria are refractory to killing by antibiotics and neutrophils, suggesting that early invasion of bacteria into deeper layers of the bladder wall may play an important role in recurrent infections.

RESULTS

Establishment of differentiated mouse bladder organoids

We generated mouse bladder organoids from C57BL/6 wild-type (WT) or mT/mG mice (Muzumdar et al., 2007), which express the red fluorescent protein tdTomato within cell membranes, following a recently published procedure (Figure 1A; Mullenders et al., 2019). We verified that these organoids recapitulate the different layers of the stratified mouse uroepithelium by comparative immunofluorescence staining of slices of bladder organoids and explanted mouse bladders. Staining with antibodies directed against uroplakin-3a (UP3a) or cytokeratin 8 (CK8) shows that cells lining the lumen of the bladder organoids strongly express both markers (Figure 1B), consistent with the staining pattern of the umbrella cell layer in mouse bladder (Figure 1C). However, we cannot rule out the possibility that some of the UP3a+ cells in the organoid might be underlying transitional bladder cells (Mysorekar and Hultgren, 2006). The presence of intermediate and basal cell layers in the bladder organoids was confirmed by staining with antibodies directed against CK13, p63, or CK7 (Figure 1B), which is also consistent with the staining patterns observed in mouse bladder (Figure 1C). In addition, CK8 staining is higher in the umbrella-like cell layer (Figure 1B, demarcated by a white dashed line) than in the underlying intermediate and basal cell layers in organoids and mouse bladder (Southgate et al., 1994). A 3D view of a bladder organoid stained with anti-CK8 antibodies confirmed that the cell layer surrounding the organoid lumen is CK8+ (Figures 1D and 1E). Bladder organoids therefore recapitulate the stratified architecture of the mouse uroepithelium, with high levels of uroplakin expression in the superficial umbrella-like cell layer, which is important for UPEC adherence and invasion (Mulvey et al., 1998).

Early invasion of UPEC into the bladder wall provides protection against antibiotics

Intravital imaging of antibiotic treatment and recovery in the infected bladder is challenging and provides limited spatiotemporal resolution (Justice et al., 2004, 2006). We therefore modeled the acute phase of a UTI by microinjecting UPEC expressing yellow fluorescent protein (YFP) into the lumen of individual bladder organoids, which mimics the natural route of infection by the urethra (Figure 2A). The infection cycle was modeled in three stages, as follows: stage one (0–165 min), an initial period of unimpeded bacterial proliferation; stage two (165–345 min), treatment with ampicillin at 10-fold the minimum inhibitory concentration (10× MIC, 64.5 μg/ml); and stage three (345–525 min), bacterial recovery after ampicillin washout. Snapshots from time-lapse imaging of two infected organoids are shown in Figures 2B–2E (Video S1) and Figures 2F–2I (Video S2), and an additional example is in Figure S1A1–7 (Video S3). We microinjected organoids with 300–1,300 colony-forming units of UPEC in a 1-nL volume (STAR Methods); the number of bacteria retained after the washing steps is about 10-fold lower. Rapid bacterial growth occurs shortly after microinjection (Figures 2B, 2C, 2F, and 2G), predominantly within the lumen (yellow arrowhead in Figure 2B). At this stage, we also identified IBC-like structures in CK8+ cells in a subset of infected organoids (Figures 3A and 3B). Hereafter, for simplicity, we shall refer to these structures as IBCs, although we acknowledge that IBC-like structures observed in the organoid model may differ in some respects from IBCs that form in the bladder wall of infected animals. In many instances, it was difficult to distinguish organoid IBCs from lumenal bacteria during time-lapse imaging. Bacterial growth was measured using an image analysis pipeline in Imaris Bitplane (STAR methods; Figure S2).

CellPress
OPEN ACCESS

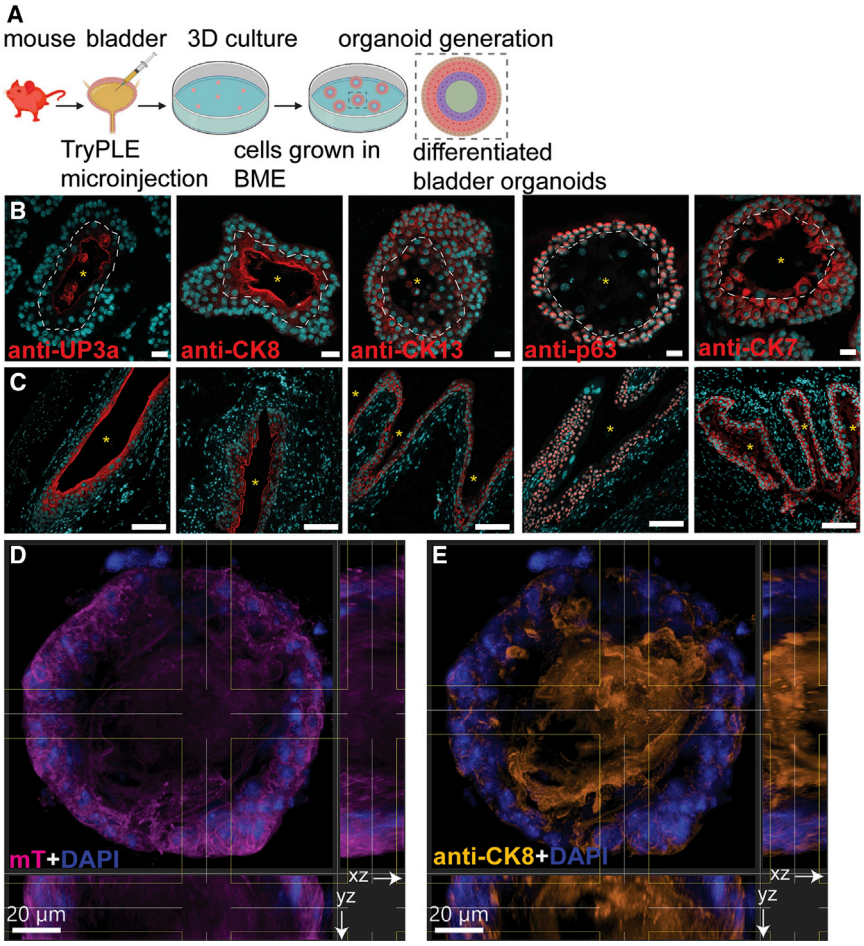

Figure 1. Mouse bladder organoids recapitulate uroepithelial stratification

(A) Schematic of the protocol for the generation of mouse bladder organoids. Lumenal cells are cultured in basement membrane extract (BME) to form differentiated bladder organoids.

(B and C) Immunofluorescence staining confirms that bladder organoids (B) recapitulate the stratified layers of the uroepithelium observed in mouse bladder tissue (C). The umbrella cell layer was identified with anti-uroplakin 3a (anti-UP3a) and anti-cytokeratin 8 (anti-CK8) antibodies. Basal and intermediate cell layers were identified with anti-CK13, anti-p63, or anti-CK7 antibodies. Cell nuclei were labeled with 4′,6-diamidino-2-phenylindole (DAPI, cyan). Yellow asterisks, lumens of the bladder organoids and mouse bladder slices. Dashed white lines, boundary between the umbrella-like and intermediate cell layers.

(D and E) Extended orthogonal section views of a 3D volume (20 × 20 × 20 μm^3) of an uninfected organoid. Uroepithelial cells are identifiable by membrane tdTomato (mT) expression (magenta) surrounding the organoid lumen in the center, including CK8+ umbrella-like cells lining the lumen. The main image, XZ, and YZ show a maximum intensity projection within this volume along the z, y, and x axes, respectively. Scale bars, 20 μm in (B), (D), and (E) and 100 μm in (C).

Addition of 10× MIC ampicillin (Figure S1B) to the medium surrounding the organoids rapidly reduces the bacterial volume within the organoid (Figures 2D and 2H), consistent with the bactericidal nature of the antibiotic. In most cases, bacterial growth resumed only after ampicillin removal (Figures 2E and S1A6 and 7). Unexpectedly, in 2 of the 124 organoids studied, slow bacterial growth continued even in the presence of the antibiotic (Figure 2I). These two distinct bacterial growth kinetics are demonstrated by representative time profiles of intraorganoid UPEC growth for the period before, during, and after ampicillin administration (Figures 2J and S1C).

A plot of intraorganoid bacterial volume over time confirms that growth is exponential (Figure 2K), with a median growth rate of 0.017 min^{-1} and doubling time of 41.5 min (Figure 2M), similar to UPEC growth kinetics in the mouse bladder (Justice et al., 2004; Scott et al., 2015). During ampicillin treatment, the bacterial volume initially increases before plateauing due to bacterial filamentation (Figure 2L). Fluorescence intensity and intraorganoid bacterial volume subsequently decline, with a median killing rate of 0.019 min^{-1} (Figure S1D). Compared to growth before ampicillin treatment, regrowth after ampicillin washout is significantly slower, with a median growth rate of 0.003 min^{-1} and doubling time of 226.8 min (Figure 2M). To rule out the possibility that delayed killing is due to insufficient or delayed drug penetration, we measured the diffusion kinetics of lucifer yellow, a hydrophilic-cell-impermeable dye with a molecular weight comparable to ampicillin, administered in the medium surrounding the organoids (Figures S1E and S1F). Mean fluorescence intensity values in the intraorganoid volume reach a maximum value of ca. 30% of the external concentration within 15–30 min of dye addition (Figure S1F). These results demonstrate that intraorganoid bacteria are rapidly exposed to high concentrations of ampicillin after its addition to the surrounding medium, presumably by diffusion of the antibiotic through the organoid wall.

Bacterial regrowth after ampicillin washout is localized exclusively to the organoid wall, in striking contrast to the preponderance of bacterial growth in the organoid lumen prior to antibiotic treatment (*cf.* Figures 2E versus 2B and 2C and Figures 2I versus 2F and 2G). At later time points (Figure 2E), the magenta staining in the interior of the organoid is an artifact of the segmentation pipeline (Figure S2) and is likely due to expansion of the lumen due to the accumulation of cell debris. We confirmed that regrowth originates from individual bacteria within the organoid wall that survive antibiotic treatment at both 10× MIC (Figures 3C and 3D; Video S4) and 2× MIC (Figures 3E and 3F; Video S5); in the latter case, a small bacterial cluster in an IBC also appears to be protected from clearance. These results suggest that the lumen may be the preferred site of bacterial growth prior to antibiotic exposure, whereas the bladder wall offers a more protective niche for bacterial survival and regrowth after antibiotic treatment.

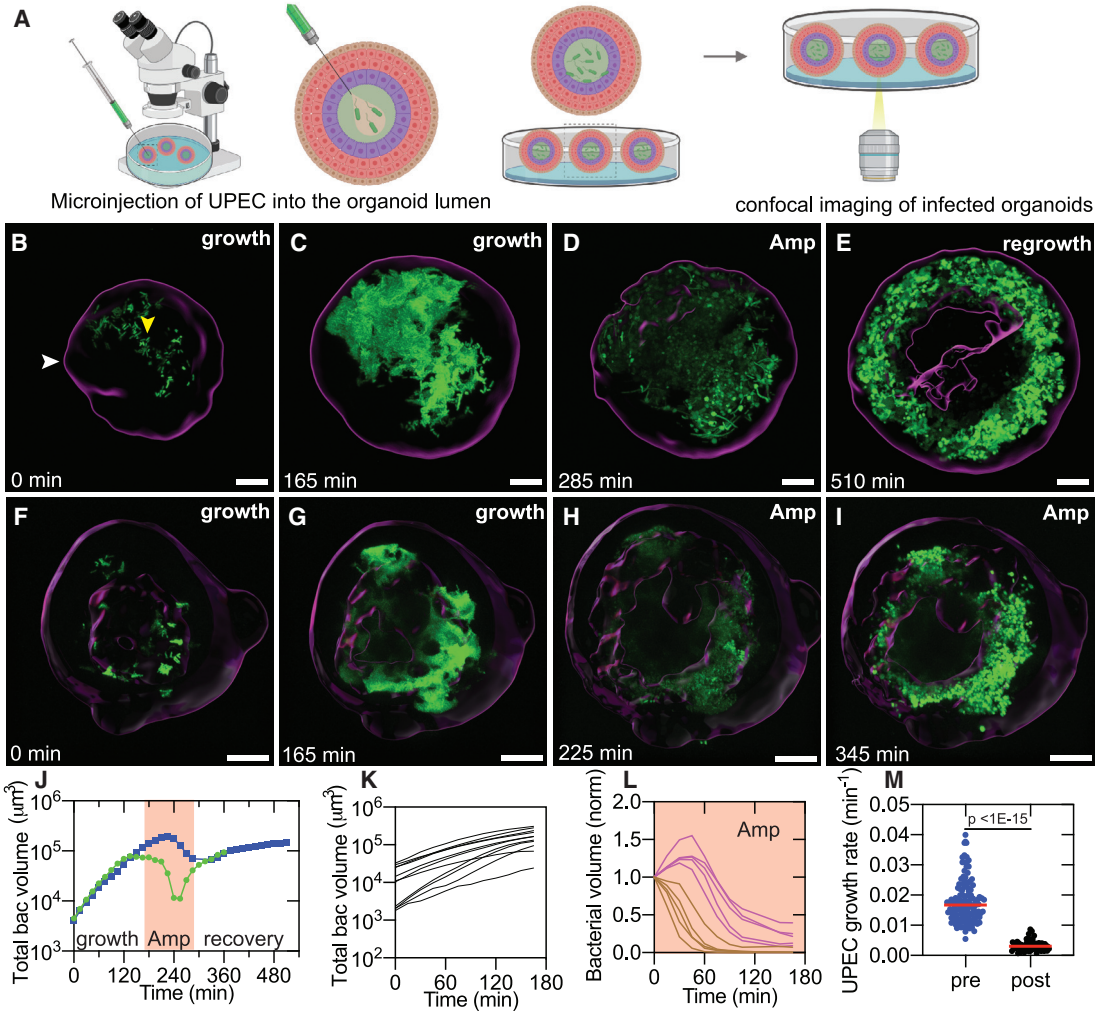

Figure 2. Bacteria within the bladder organoid wall are refractory to antibiotic clearance

(A) Schematic of the microinjection protocol. Bacteria are injected by a glass microcapillary into the lumen of individual organoids, which are resuspended in a collagen matrix for live-cell confocal imaging.

(B–E) Snapshots from time-lapse imaging of an infected organoid over 9 h. (B) The volume of bacterial fluorescence within the organoid increases rapidly during the initial growth phase (0–165 min from the start of the experiment in B and C), predominantly within the lumen. White arrowhead, organoid boundary. Yellow arrowhead, lumenal bacteria. (D) The intraorganoid bacterial volume decreases after addition of 10× MIC ampicillin to the culture medium (ca. 165–345 min). (E) Bacterial regrowth is restricted to the organoid wall in the recovery phase after antibiotic withdrawal (ca. 345–525 min; Video S1).

(F–I) An unusual example where the bacterial volume initially decreases (*cf.* H versus G) but subsequently increases (I) even in the presence of antibiotic (Video S2).

(J) Time profiles of intraorganoid bacterial volume over time the organoids in (B)–(E) (squares) and (F)–(I) (circles). Shaded region, period of antibiotic treatment.

(K–M) Bacterial growth dynamics at different stages of infection. (K and L) Representative plots of bacterial volume versus time show exponential growth during the growth phase (K; n = 11 biological replicates) and exponential decay during antibiotic treatment (L; n = 10 biological replicates). Bacterial volume typically declines immediately after antibiotic administration (L; brown lines), but in some instances, growth continues for some time before declining (L; magenta lines). (M) Scatterplot for the growth rate of the bacterial volume within the bladder organoids before (n = 124 biological replicates) and after (n = 58 biological replicates) antibiotic exposure. ($p < 1E-15$, Mann-Whitney test). Red lines, median values. Scale bars, 50 µm in (B)–(I).

Neutrophils swarm toward intraorganoid UPEC with three distinct migratory profiles

Organoids are powerful systems with which to study immune cell responses *in situ* (Nikolaev et al., 2020; Sachs et al., 2019; Yuki et al., 2020) and to visualize the spatiotemporal dynamics of immune cell responses by long-term live-cell imaging. Peripheral innate immune cells such as neutrophils have been shown to be the first responders in the early phases of bladder infection in the mouse model (Haraoka et al., 1999). We therefore added Ly6G+ (Figures S3A–S3C) and CD11b+ (Figures S3D–S3F) murine bone-marrow-derived neutrophils to the collagen matrix surrounding bladder organoids immediately after microinjection of the organoid lumen with UPEC. Neutrophils were pre-labeled with CellTracker dye to facilitate identification (Figures S3B and S3E) and incubated with murine granulocyte colony stimulating factor (G-CSF) during

CellPress
OPEN ACCESS

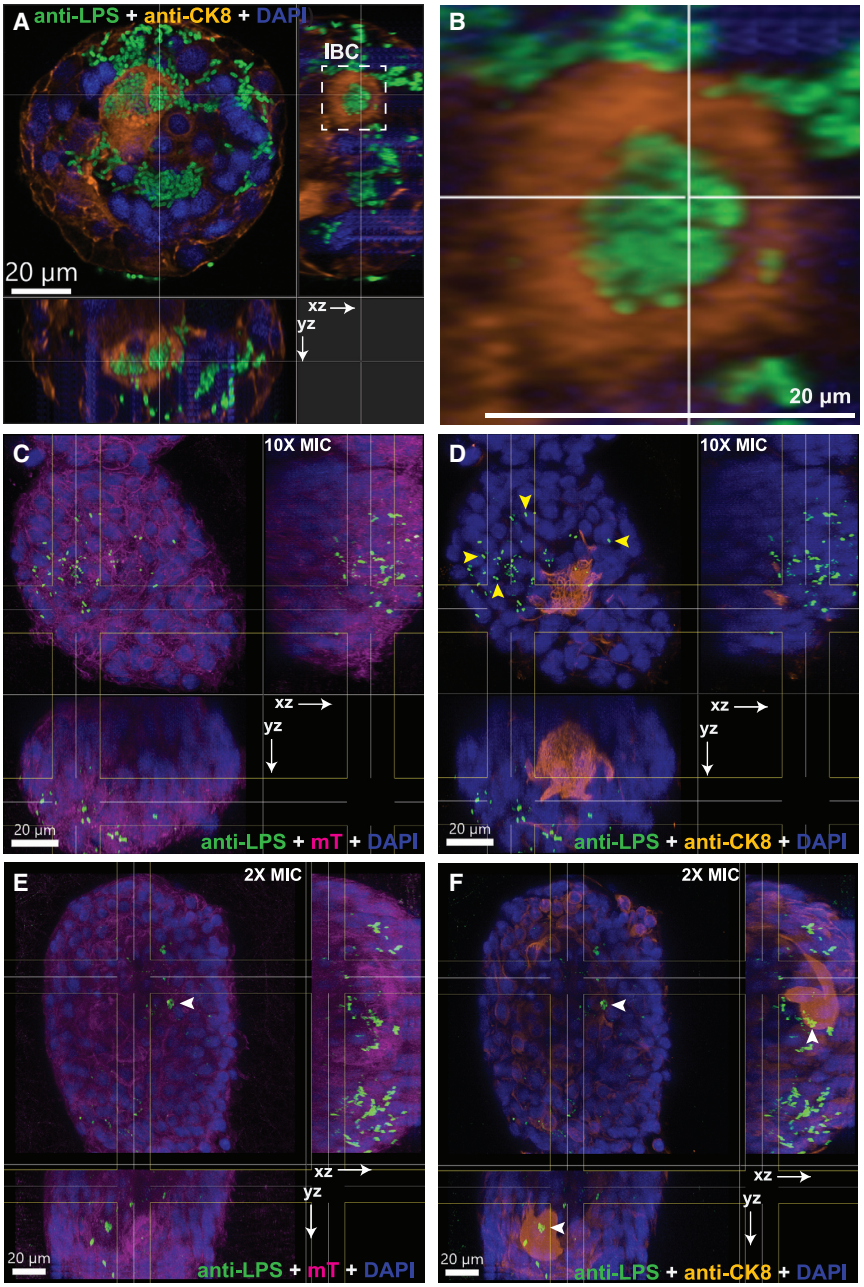

Figure 3. Survival and post-antibiotic regrowth of solitary bacteria within the bladder wall

Bacteria are labeled with an anti-LPS antibody (green).

(A) Orthogonal sections of an infected organoid. Dashed white line, IBC within a CK8+ cell.

(B) Zoomed-in image of the IBC confirms bacteria within a CK8+ cell. Cell nuclei were labeled with DAPI (blue).

(C–F) Orthogonal section views of a 3D volume (20 × 20 × 20 μm^3) within the organoid wall of infected organoids after ampicillin treatment at 10× MIC (C and D) or 2× MIC (E and F). The main image, XZ, and YZ show a maximum intensity projection within the volume along the z, y, and x axes, respectively. (C and E) Magenta, mT labeling of the uroepithelial cells. (D and F) Amber, CK8 staining. (D) Yellow arrows, examples of solitary bacteria in the organoid wall. (E and F) White arrowheads, example of a bacterial clump within CK8+ cells. Scale bars, 20 µm.

co-culture to promote maturation. Live-cell imaging revealed three distinct patterns of neutrophil migration dynamics (Videos S6, S7, and S8). To quantify the dynamics of migration, we used an image analysis pipeline described in Figure S4.

In most cases, neutrophils surrounding an infected organoid migrate toward and accumulate in the lumen, forming aggregates or swarms (Figures 4A1–3 and 4B1–3). Neutrophil migration into the organoid lumen is consistently accompanied by a sharp reduction in bacterial volume (Figures 4A2–5, 4B2–5, and 4C2–5). In some cases, the neutrophil swarms remain within the lumen for >30 min (Figures 4A3–5 and S5D1–D5), which is characteristic of persistent swarms (Kienle and Lämmermann, 2016; Lämmermann et al., 2013; Reátegui et al., 2017). In other cases, the swarm rapidly disaggregates after clearance of intraorganoid bacteria (Figures 4B3–5 and S5E1–5), which is characteristic of transient swarms. In a third category, large intraorganoid aggregates of neutrophils do not form; rather, neutrophil numbers within the organoid fluctuate in response to bacterial numbers (Figures 4C1–5 and S5F1–5). We classify this third category, with fluctuating neutrophil numbers inside the infected organoid, as dynamic swarms (Hopke et al., 2020).

The migration of neutrophils into infected organoids is also indicated by a change in cell shape, as neutrophils surrounding the organoid are predominantly spherical, whereas migratory neutrophils adopt elongated shapes (Figure S5O). Importantly, neutrophils do not migrate toward uninfected bystander organoids (Figures 4A and 4B; quantified in Figures S5M and S5N), which confirms that neutrophils can discriminate between uninfected and infected organoids and direct their movement specifically toward infected organoids. These neutrophil dynamics are exemplified by time profiles of the neutrophil volume surrounding the organoid, neutrophil volume within the organoid, and intraorganoid bacterial volume. Data for each parameter are shown in Figures 4D–4F (corresponding to Figures 4A1–5, 4B1–5, and 4C1–5) and Figures S5G–S5I (corresponding to Figures S5D–S5F); absolute numbers are shown in Figures S5A–S5C and Figures S5J–S5L. Infected bladder organoids therefore reproduce the range of neutrophil migratory responses reported from

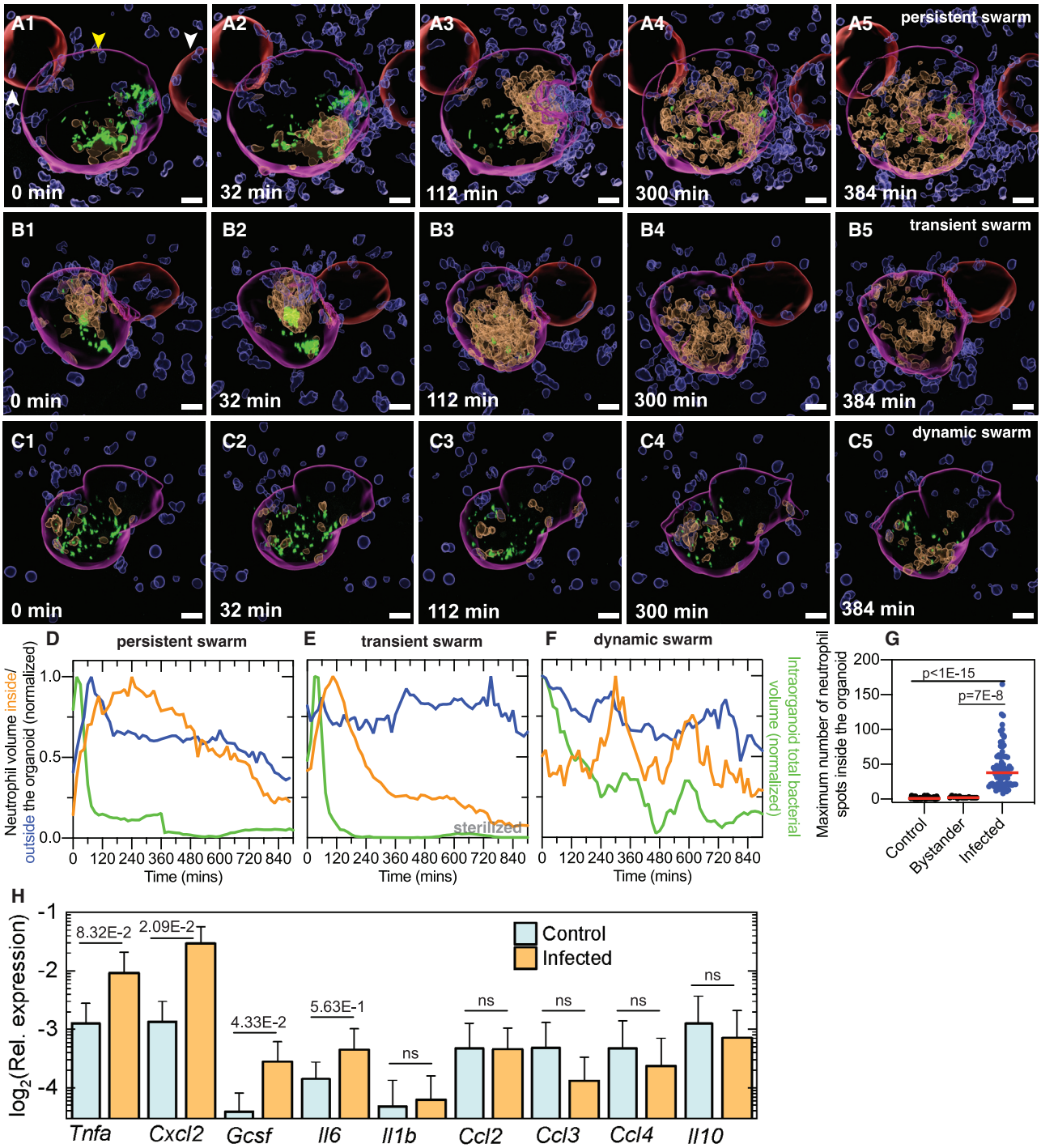

Figure 4. Neutrophil swarming dynamics in response to bacterial infection

(A1–C5) Surfaces of intraorganoid (amber) and extraorganoid (blue) neutrophils and infected (magenta) and uninfected (red) organoids were generated using a Bitplane Imaris analysis pipeline. UPEC (green) is shown without processing to identify individual bacteria. Scale bars, 20 μm. (A1–A5) Persistent swarm. Snapshots show the migration of neutrophils into the lumen of an infected organoid (yellow arrowhead) but not the adjacent uninfected organoid (white arrowhead). A neutrophil swarm forms around the bacteria in the lumen and persists during the experiment. Solitary bacteria in the bladder wall (A5) appear to be refractory to clearance. Images are presented in a perspective view. (B1–B5) Transient swarm. The image series shows two consecutive cycles of neutrophil swarm formation and disaggregation in response to intraorganoid bacterial growth. (C1–C5) Dynamic swarm. The image series shows rapidly fluctuating neutrophil numbers within the organoid without the formation of large aggregates.

(legend continued on next page)

intravital imaging studies, and lumenal bacteria are effectively cleared by incoming neutrophils independently of their migratory profile.

We characterized mixed populations of infected and bystander organoids relative to uninfected organoids at ca. 4 h post-infection by measuring the expression of genes that could stimulate leukocyte migration and genes that are known to be upregulated during UPEC infection *in vivo* (Figure 4H). We found that expression of the inflammatory cytokine *Tnfa* (Yu et al., 2019), neutrophil maturation factor *Gcsf* (Ingersoll et al., 2008; Semerad et al., 2002), and neutrophil chemoattract *Cxcl2* (Sundac et al., 2016) were more highly expressed in infected and bystander organoids than uninfected controls (Sundac et al., 2016). A small but statistically insignificant increase was observed in the expression of inflammatory cytokine *Il6*. No change in expression was observed for macrophage-specific chemokines such as *Ccl2*, *Ccl3*, or *Ccl4*, which also stimulate neutrophil migration but are typically produced by resident macrophages (Lacerda Mariano et al., 2020; Schiwon et al., 2014). These observations are consistent with the cellular composition of the organoids as well as results from the mouse model, in which UPEC infection does not increase *Ccl3* expression and increases *Ccl4* expression only at later stages of infection (Ingersoll et al., 2008). These infection-driven changes in host-cell gene expression could partly explain the directed migration of neutrophils toward infected organoids.

Bacteria within the bladder organoid wall are refractory to clearance by neutrophils

The rapid clearance of lumenal bacteria by migratory neutrophils provides an opportunity to observe niches where bacteria may be protected from neutrophil attacks, such as IBCs (Justice et al., 2004). Figure 5A1–3 shows an example of an organoid IBC that forms and persists despite the presence of a persistent swarm of neutrophils within the organoid that successfully clears the lumenal bacteria. Snapshots from the raw images at the corresponding time points are shown in Figures S3G and S3H to confirm that the IBC is formed within a uroepithelial cell. Live-cell imaging revealed the IBC to be a dynamically fluctuating structure; for example, in the 15-min interval between Figure 5A3 and 4 (Video S9), the IBC begins to shed bacteria, which are rapidly taken up by nearby neutrophils. Most of the bacteria released from the IBC are processed and killed within 30 min, as evidenced by the loss of YFP fluorescence (Figure 5A5). In contrast, Figure 5B1–5 (Video S10) shows another example of an IBC that forms in the presence of a persistent neutrophil swarm (Figure 5B1 and 2, white arrowhead), but in this case, the bacteria shed from the IBC are spread by the neutrophils to different regions of the bladder epithelium (Figure 5B3 and 4, cyan arrowheads). Some of these bacteria persist as isolated bacteria within the organoid wall and appear to resist clearance by neutrophils (Figure 5B5, cyan arrowheads).

Unexpectedly, at early time points, we also identified spatially isolated subpopulations of bacteria, comprising individual cells or small clusters (threshold of detection set at 10 μm^3), located within the organoid wall (Figure 5B1, yellow arrowheads). Hereafter, we refer to these subpopulations as solitary bacteria to distinguish them from communal bacteria within IBCs. The high spatiotemporal resolution afforded by confocal imaging allowed us to track three examples of solitary bacteria over the course of the time series shown in Figure 5B1–B5. Our results confirm that solitary bacteria are located within the organoid wall throughout the time course, and they appear to be refractory to neutrophil-mediated clearance (Figure 5B5, yellow arrowheads). At later time points, the number of solitary bacteria was increased by the addition of bacteria shed by a ruptured IBC (Figure 5B5, cyan arrowheads). Even 15 h after addition of neutrophils, solitary bacteria persist within some organoids (Figures 5C3 and 4, 4A, and 4C; analysis in Figures 4D, 4F, S5A, S5C, S5G, and S5J), whereas other organoids are successfully sterilized by the neutrophils (Figure 5C1 and 2; analysis in Figures 4E, S5B, and S5H–S5L). Persistence (Figure 5D) and sterilization occur with roughly equal frequency. Live-cell imaging confirmed that bacteria shed from IBCs contribute only a small fraction of these solitary and persistent bacteria.

These results demonstrate that niches within the deeper layers of the bladder epithelium, below the superficial layer of umbrella-like cells containing IBCs, can also harbor subpopulations of bacteria that are resistant to clearance by antibiotics or neutrophils, independent of the migratory profile of the neutrophil swarm (Figure 5C3 and 4). We attempted to localize these persistent bacteria with greater precision, but the spatial resolution of confocal microscopy was insufficient to unambiguously identify the boundaries of the bladder lumen and the precise location of individual bacteria within the organoid wall.

Volumetric EM reveals five distinct bacterial niches within infected organoids

Technical advances in electron microscopy (EM) now permit volumetric imaging of large samples using SBEM (Denk and Horstmann, 2004; Hoffman et al., 2020; Maclachlan et al., 2018). We used SBEM to image an entire infected organoid at ca. 6 h after microinjection of UPEC and addition of neutrophils. The organoid was imaged with optical microscopy (Figure S6A) prior to staining and resin embedding. Serial images of the entire structure were collected at a lateral resolution of 30 nm with 100-nm sections separating each image; examples of slices are shown in Figure S6B1–4. High-contrast staining of SBEM

(D–F) Time profiles of the relative volumes of neutrophils within the organoid, neutrophils surrounding the organoid, and bacteria within the organoid for the profiles presented in (A)–(C), respectively. In each case, the volume is normalized to the maximum volume during the the experiment. Persistent and transient swarms are characterized on the basis of neutrophil reverse migration rates.

(G) Scatterplots of the maximum number of intraorganoid neutrophils during the experiment in uninfected control organoids (n = 30 biological replicates), uninfected bystander organoids (n = 15 biological replicates), and infected organoids (n = 75 biological replicates). Red lines represent median values.

(H) Plot of the expression of inflammatory cytokines and chemokines relative to *Gapdh* in uninfected and infected organoids. Bars represent mean values; error bars represent standard deviations (n = 4 biological replicates per condition, each replicate comprising 75–100 infected organoids within a population of 750–1,000 organoids). p values were calculated using a Mann-Whitney test (G) or a Kruskal-Wallis ANOVA test (H).

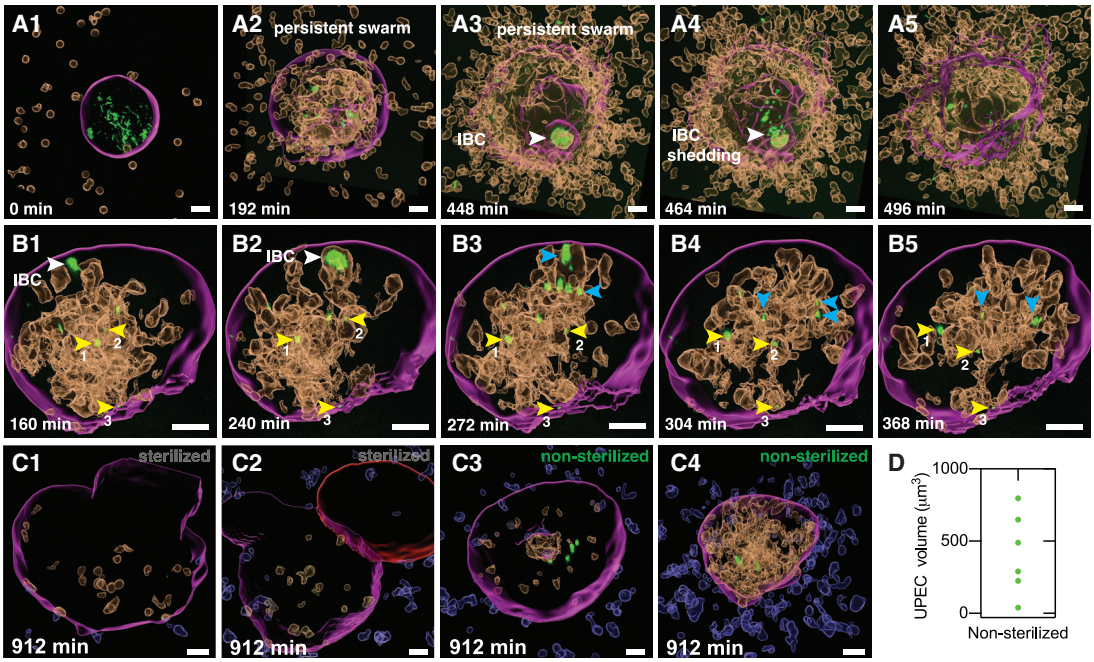

Figure 5. Bacteria within the bladder organoid wall are protected from clearance by neutrophil swarms

(A1–A5 and B1–B5) Two examples of IBCs that are protected from neutrophil-mediated clearance. Shedding of bacteria from an IBC (A4, A5, B2, and B3) is followed by phagocytic uptake and rapid clearance (A5) or dispersal to other niches in the bladder epithelium (B5, cyan arrowheads). Three examples of isolated solitary bacteria in the bladder wall (yellow arrowheads labeled 1, 2, and 3) that are refractory to clearance throughout the time series in (B1)–(B5).

(C1–C4) Snapshots at ca. 15 h after infection and addition of neutrophils. (C1 and C2) Examples of bacterial clearance from organoids following exposure to neutrophils. (C3 and C4) Examples of bacterial persistence in organoids where the neutrophil swarm disperses (C3) or persists up to 15 h post-infection (C4). (A1–C4) Scale bars, 20 μm.

(D) Total bacterial volume at 15 h post-infection in non-sterilized organoids (n = 6 biological replicates).

samples densely labels cell membranes, which allowed us to identify cell membranes and to localize all bacteria within the organoid. In addition, optical microscopy imaging prior to embedding provided a 3D map of the organoid, which facilitated the identification of fluorescently labeled cells such as neutrophils in the final EM image series. We identified a total of 2,938 bacteria and classified them into 5 distinct subpopulations according to their locations within the organoid (Figures 6A–E and S6B1–4).

Most (62%, n = 1,821) of the bacteria are extracellular and located within the organoid lumen (Figures 6A and S6B1). Smaller bacterial fractions are located either as solitary bacteria within the cytoplasm of bladder epithelial cells (3.8%, n = 111) or within the IBC (13.5%, n = 398) (Figures 6C, 6D, and S6B2–3). The small fraction of bacteria located within neutrophils (4.8%, n = 141) is likely an underestimate because bacteria are degraded after phagocytosis (Figures 6B and S6B2). Bacteria within the neutrophils have an altered morphology, likely due to exposure to antimicrobial stresses within the neutrophil. We identified a fifth subpopulation of solitary bacteria, which we classify as "pericellular" (15.9%, n = 467), which is located between bladder epithelial cells within the organoid wall (Figures 6E and S6B4). To the best of our knowledge, this pericellular subpopulation of solitary bacteria has not been reported previously, presumably due to the difficulty of whole-bladder imaging with sufficient spatial resolution to identify individual bacteria located between host-cell membranes.

A view inside a model of the organoid, created from a 3D map of coordinates of all cells and bacteria, shows the arrangement of the different bacterial subclasses (Figure 6F; Video S11). The bacterial subpopulation within the irregularly shaped lumen clusters toward the first quadrant (zoomed-in image of Figure 6G), likely indicating the site of microinjection. Intracellular and pericellular solitary bacteria can be found scattered throughout all areas of the organoid wall (zoomed-in image of Figure 6H). Individual neutrophils can be observed in all areas of the organoid wall as well as the lumen (Figure 6H), and some of these neutrophils contain bacteria (Figure S6F). Bacteria within the IBC form a tight cluster below the nucleus of the cell hosting the IBC (Figure 6F). Protection of intracellular bacteria from phagocytic uptake is evident from the fact that the IBC remains intact despite the infected cell being surrounded by multiple neutrophils. A plot of the shortest distance of each subpopulation to the organoid lumen is shown in Figure 6J. Intracellular and pericellular solitary bacteria are found within deeper layers of the organoid that express intermediate and basal cell markers (Figure 1B).

We asked whether the intracellular and pericellular solitary subpopulations are phenotypically different from bacteria in the organoid lumen. UPEC has been shown to alter flagellar expression and cell shape during bladder infection (Anderson et al., 2004; Lane et al., 2007; Wright et al., 2007). We therefore used immunofluorescence to probe flagellin expression *in situ*.

CellPress
OPEN ACCESS

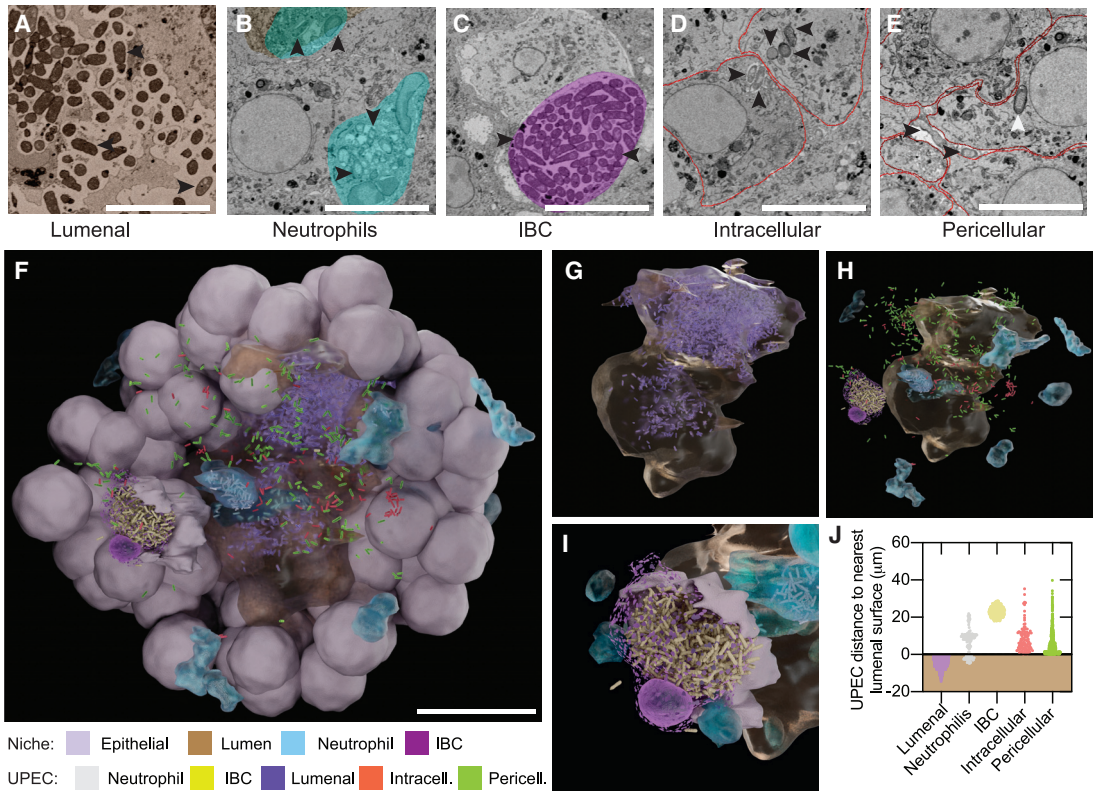

Figure 6. Volumetric electron microscopy reveals five distinct bacterial niches within an infected organoid

(A–E) SBEM snapshots of an infected organoid at ca. 6 h after microinjection of UPEC and addition of neutrophils. Black arrowheads, bacteria within each of the five distinct niches. (A) Extracellular bacteria within the organoid lumen (brown; n = 1,821). (B) Bacteria within neutrophils (light cyan) in the lumen or bladder wall (n = 141). (C) Bacteria within an IBC (purple; n = 398). (D) Individual intracellular bacteria within the cytoplasm of epithelial cells (cell boundaries in red; n = 111). (E) Individual pericellular bacteria located between epithelial cells (n = 467). White arrowhead, an additional example of an intracellular bacterium.

(F) 3D model derived from serial electron microscopy images of the entire organoid. The model shows the interior of the organoid with lumen (brown), epithelial cells (gray), and neutrophils (cyan). The five bacterial subpopulations corresponding to (A)–(E) are colored violet (lumenal), gray (neutrophil), yellow (IBC), red (intracellular), or green (pericellular). Organoid diameter, 85 μm. Scale bars, 5 μm in (A)–(E) and 20 μm in (F).

(G) Zoomed-in image of extracellular bacteria in the lumen (brown).

(H) Zoomed-in image of all other bacterial subpopulations outside the lumen.

(I) Zoomed-in image of bacteria within the IBC that are protected from clearance by the surrounding neutrophils.

(J) Scatterplot of the distance of each bacterial subpopulation from the lumenal surface (the shaded brown region indicates the lumen).

Because paraformaldehyde fixation tends to degrade the fluorescence signal from bacterial YFP, we used immunostaining against lipopolysaccharide (LPS) and a mask of the organoid shape to label intraorganoid bacteria and bacteria surrounding the organoid (Figure 7A). The corresponding image with anti-flagellin immunostaining (Figure 7B) shows that most intraorganoid bacteria have low or no detectable flagellin expression. The specificity of the anti-flagellin antibody was confirmed using a flagellin-deficient Δ*fliC* strain (Figure S6D). By applying a volume threshold to the intraorganoid bacterial clusters, we found that large bacterial clusters (volume, >1,000 μm^3) express very low flagellin levels (Figure 7D), whereas smaller clusters and individual bacteria retain intermediate to high levels of flagellin (Figures 7C and S6E). Thus, intraorganoid bacteria that express flagellin are predominantly single cells or small clusters located within the organoid wall; both observations suggest that these subpopulations correspond to the intracellular or pericellular subpopulations of solitary bacteria identified in our serial electron micrographs. This point is strengthened by our observation that bacteria within the IBC have severely reduced flagellar expression, as shown previously in infected mice (Wright et al., 2005), whereas single bacteria surrounding the IBC retain a high level of flagellar expression (Figure 7E).

Scanning EM (SEM) is a powerful technique with which to examine surface morphology and overall bacterial shape. We ruptured open an infected organoid by using a tungsten needle (Heo et al., 2018) at ca. 6 h after microinjection with UPEC to gain access to the interior of the organoid (Figure 7F). We found that most bacteria accessible to SEM imaging are located within tight clusters, which is suggestive of IBC growth (Figures 7G and 7H). These bacteria are coccoid in shape and are not flagellated (Figure 7H), consistent with previous findings in infected mice (Anderson et al., 2003; Justice et al., 2004). In contrast, we identified a small subpopulation of bacteria in a different spatial location within the organoid that retain flagellar expression (Figures 7I and 7J), consistent with data in Figures 7C and 7D. We verified

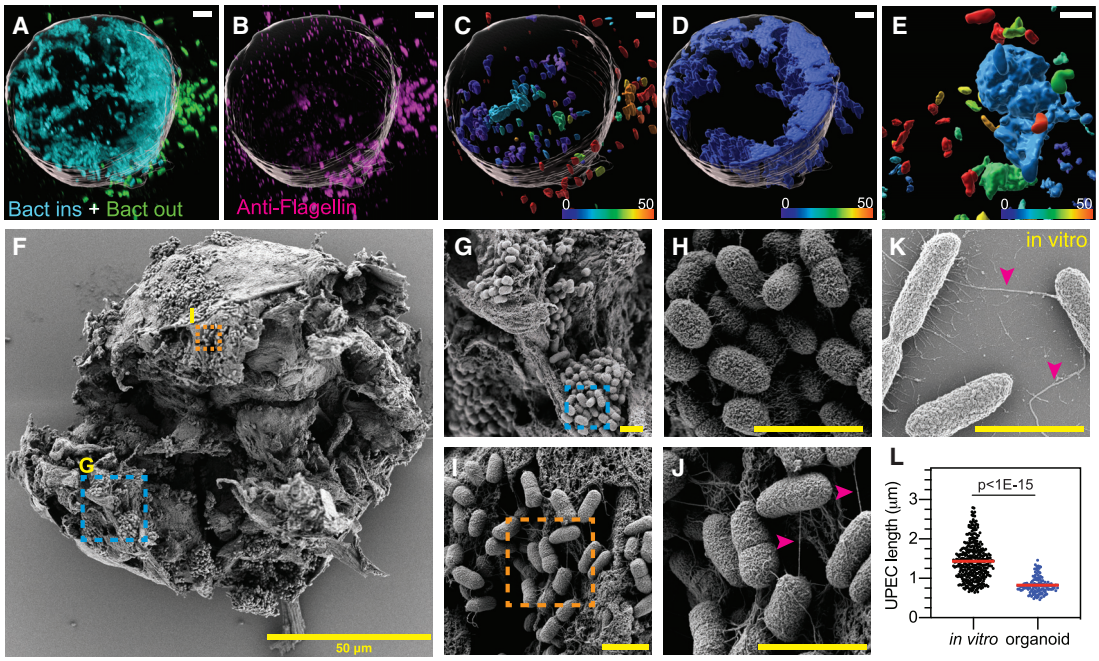

Figure 7. Solitary bacteria within the bladder organoid wall are rod shaped and flagellated, whereas bacteria within clusters are coccoid and non-flagellated

(A–D) Perspective views of an infected organoid (surface in gray) at ca. 6 h after microinjection with UPEC. (A) Bacteria inside (cyan) and outside (green) the organoid identified by anti-LPS staining. (B) Flagellated bacteria (magenta) identified by anti-flagellin staining.

(C–E) Co-expression of LPS and flagellin for individual bacteria (C) or large bacterial clusters, which are predominantly restricted to the lumen (D). Bacteria are color-coded based on the intensity of the flagellin signal. Flagellated bacteria are predominantly observed outside the organoid (C) but also occur as solitary cells within the organoid wall. (E) Bacteria within an IBC exhibit low levels of flagellin. Solitary bacteria surrounding the IBC retain high levels of flagellin.

(F) SEM image of an infected organoid at 6 h after microinjection with UPEC. Ruptured organoids reveal multiple areas of bacterial growth. Zoomed-in images for two representative areas are shown in (G)–(J).

(G and H) Bacteria are tightly packed, coccoid shaped, and flagellin negative (H).

(I and J) Bacteria are loosely packed, rod shaped, and flagellin positive (J; magenta arrowheads).

(K) SEM image of UPEC grown in axenic culture. Cells are rod shaped and flagellated (magenta arrowheads). Scale bars, 5 μm in (A)–(E) and 2 μm in (G)–(K).

(L) SEM-derived size distributions for bacteria grown to stationary phase in axenic culture (n = 370) and bacteria within tightly packed clusters in the organoid (n = 136). ($p < 1E-15$, calculated using a Mann-Whitney test).

that bacteria from a stationary-phase axenic culture retain flagellin expression (Figure 7K) and are longer than intraorganoid bacteria (Figure 7L). Thus, the bladder organoid model recapitulates characteristic morphological features of bacteria within IBCs as well as distinct niches in the bladder wall in which the bacteria are rod shaped and flagellated. These observations provide a more comprehensive picture of UPEC phenotypic variants that arise during the course of infection.

DISCUSSION

The mouse model of UPEC infection faithfully reproduces key features of UPEC pathogenesis in humans (reviewed in Flores-Mireles et al., 2015 and Hung et al., 2009), but the complexity of this model poses difficulties for live-cell imaging with high spatiotemporal resolution. There is also a paucity of tractable *in vitro* models that reproduce the complex 3D-stratified architecture of the bladder wall and key features of the UPEC pathogenesis cycle, such as bacterial persistence and regrowth after antibiotic treatment. In an early study, stratified uroepithelial layers were generated from a human cancer cell line grown on collagen beads by exposure to shear stress (Smith et al., 2006). However, this model lacks a lumen where bacteria can be introduced in a topologically correct manner. In another model, a virus-immortalized human bladder cell line was cultured under flow to mimic micturition, but this model does not include a stratified uroepithelium or the ability to introduce additional cell components such as immune cells (Andersen et al., 2012). In a more recent study, primary human uroepithelial cells were grown as stratified layers on Transwell inserts; however, in this model, stratification is non-uniform and it is difficult to monitor immune cell dynamics using live-cell imaging (Horsley et al., 2018). Although several stratified bladder epithelium models have been described (Cattan et al., 2011; Chabaud et al., 2017; Halstead et al., 2017; Kim et al., 2020; Shin et al., 2011; Suzuki et al., 2019), to the best of our knowledge, in only one recent example has an advanced organoid model been used to model UPEC pathogenesis (Kim et al., 2020). Although the latter study reported epithelial cell injury and IBC formation following UPEC infection, consistent with our observations and previous results from the mouse model, the dynamics of these changes were not reported.

Here, we show that bladder organoids embedded in a collagen matrix fulfill all of these requirements, namely, the ability to track bacterial growth within the organoid wall and a central lumen that mimics the bladder volume; the ability to add and remove soluble compounds, which we exploit for real-time analysis of bacterial responses to antibiotic treatment; and the ability to study the directed migration of immune cells into organoids in response to infection. Organoids are amenable to long-term live-cell imaging and offer a medium-throughput format with the flexibility to combine different cell types, such as uroepithelial cells and immune cells derived from different strains of genetically modified mice. These combinations are not possible in simple monolayer systems (Andersen et al., 2012) or in previously reported complex stratified systems (Horsley et al., 2018; Smith et al., 2006). In these respects, the organoid model also offers advantages compared to experiments with explanted bladder tissue (Justice et al., 2004, 2006). Shortcomings of the organoid model in its current form include the absence of resident immune cells (Lacerda Mariano et al., 2020; Schiwon et al., 2014) or vasculature (Homan et al., 2019; Mansour et al., 2018), the accumulation of cell debris in the lumen, and the inability to expose the cells of the umbrella-like layer facing the lumen to urine. Some of these limitations may be addressed with a bladder-chip platform (Sharma et al., 2021) or through the development of organoid-on-chip systems (Park et al., 2019; Takebe et al., 2017; Zhang et al., 2018).

We leverage these advantages to demonstrate that whereas the bladder organoid lumen is the predominant site of bacterial replication, it is the simultaneous presence of bacteria within the organoid wall that enables infection to resist clearance by antibiotics and neutrophils. Prior to antibiotic treatment, rapid growth of bacteria in the organoid lumen predominates, although widely scattered invasion of bacteria into the bladder wall occurs at the same time. Some of the invading bacteria take up residence within the superficial umbrella-like cells abutting the organoid lumen, where they replicate intracellularly to form IBCs, whereas others invade into deeper layers of the organoid wall. Bacteria within IBCs are communal, non-flagellated, coccoid shaped, and intracellular. In contrast, bacteria that invade into deeper layers of the organoid wall are solitary, flagellated, rod shaped, and intracellular or pericellular. Following antibiotic washout, the spatial pattern of bacterial growth is reversed, occurring at scattered sites throughout the organoid wall but only rarely within the lumen. Bacterial regrowth in the organoid wall after antibiotic treatment is significantly slower than growth in the organoid lumen prior to treatment. In rare cases, we found that bacteria within the organoid wall continue to divide even in the presence of antibiotic. This observation could reflect a niche within the organoid wall where antibiotic penetration is poor, emergence of antibiotic resistance, or the fact that bacterial responses to antibiotics are heterogeneous and dynamic and may, in some cases, reflect balanced division and death (Wakamoto et al., 2013). These dynamic and transient phenotypes are difficult to capture in animal models or using conventional static measurements of bacterial numbers such as colony forming units. We conclude that early invasion of solitary bacteria into deeper layers of the bladder wall, concomitant with invasion of superficial umbrella cells and IBC formation, may play an important role in bacterial persistence and relapse following antibiotic treatment.

We observed similar spatially distinct dynamics for bacterial killing by neutrophils. The small volume and spherically symmetric geometry of the organoid model allowed us to image and quantify neutrophil migration dynamics, which would be difficult to achieve in Transwell-based models. We found that UPEC infection of organoids generates a strong and highly directed neutrophil migration response, with three distinct spatiotemporal patterns (persistent, transient, or dynamic) that are reminiscent of descriptions based on intravital imaging of neutrophil responses to bacterial infections (Hopke et al., 2020; Isles et al., 2019; Kienle and Lämmermann, 2016; Lämmermann et al., 2013; Liese et al., 2013; Poplimont et al., 2020; Shannon et al., 2013), and relative frequencies of these behaviors may differ *in vivo* due to the presence of a complete resident immune system. We also found that neutrophils migrate out of the lumen of bladder organoids after resolving infection. Regardless of the neutrophil migration pattern, about half of the organoids that we studied were not completely sterilized by neutrophils even after many hours. In most of these cases, bacterial survival was restricted to the organoid wall while lumenal bacteria were sterilized.

Although both IBCs in superficial umbrella-like cells and solitary bacteria within deeper layers of the organoid wall appear to be relatively refractory to clearance by neutrophils, we found that the bacteria released when IBCs rupture are rapidly taken up and destroyed by patrolling neutrophils. In a subset of organoids where we did not detect any IBCs, solitary bacteria within deeper layers of the uroepithelium were solely responsible for survival during neutrophil attacks. Although we observed both pericellular and intracellular solitary bacteria by SBEM, it is possible that the intracellular population is better situated to survive attacks by neutrophils or other resident immune cells. The organoid model may exaggerate the numbers of solitary bacteria due to the lack of resident macrophages or the insufficient maturation and activation of bone-marrow-derived neutrophils in the model. Nevertheless, these observations suggest that early and IBC-independent invasion of solitary bacteria into deeper layers of the bladder wall might play an important role in recurrent infections by generating a subpopulation that is refractory to clearance by antibiotics and the host innate immune response.

Solitary bacteria in deeper layers of the bladder wall are phenotypically distinct from bacteria within IBCs, inasmuch as they are rod shaped and flagellated, whereas bacteria within IBCs are coccoid shaped and non-flagellated. The latter point is interesting because the loss of flagellar expression within IBCs has been reported previously (Wright et al., 2005), whereas flagellar expression has been shown to be important for generating persistent infections in the mouse bladder (Lane et al., 2007; Wright et al., 2005). Our findings suggest that non-flagellated bacteria within IBCs and flagellated solitary bacteria seeded throughout deeper layers of the bladder wall may both contribute to survival during antibiotic treatment and neutrophil attacks. Given the relatively small numbers of solitary bacteria in the deeper layers of the organoid wall, it is unlikely that this subpopulation could be identified using population-averaged

measurements, such as transcriptomic analysis of the total bacterial population within the bladder, or by non-exhaustive microscopic imaging of bladders from infected mice.

The small volume of the organoid lumen and the lack of bacterial clearance by micturition might accelerate the formation of IBCs relative to the mouse model. Even so, it is noteworthy that spatially distinct IBCs and solitary bacteria within deeper layers of the organoid wall both appear within hours of infection. This contrasts with the current model of UPEC persistence, which postulates that cycles of formation and rupture of IBCs, resulting in exfoliation of superficial umbrella cells and exposure of underlying layers of the stratified epithelium, are a precursor to invasion of bacteria into deeper layers of the uroepithelium. QIRs are thought to arise from bacteria in deeper layers of the bladder wall (Mysorekar and Hultgren, 2006). At present we cannot rule out the possibility that QIRs and solitary bacteria in deeper layers of the bladder wall, as described here, are phenotypically equivalent. Although these populations seem to arise on different timescales, it may be that the barrier to invasion of the bladder wall is less robust in the organoid model than in the mouse bladder, permitting earlier colonization of deeper layers. Alternatively, it is possible that early invasion of bacteria into deeper layers of the bladder wall may have been overlooked in previous studies in infected mice due to the difficulty of detecting small numbers of isolated bacteria within a large mass of tissue.

The dynamics of host-pathogen interactions during bladder infections are difficult to capture with high spatiotemporal resolution in conventional animal models. Bladder organoids, being miniaturized and experimentally tractable models of the bladder, are well positioned to generate new insights into UPEC pathogenesis, although it is important to note that organoid models lack the full complexity of the *in vivo* tissue environment. Thus, we view the two models, animal and organoid, as complementary approaches with distinct advantages and disadvantages. Here, we use time-lapse optical microscopy and EM to demonstrate the existence of solitary subpopulations of intracellular and pericellular bacteria located within deeper layers of the stratified bladder organoid wall, beneath the superficial layer of umbrella cells. These solitary subpopulations appear early in the course of infection, concomitant with the formation of IBCs in the umbrella cell layer, and they resist elimination by antibiotics and neutrophils. Improved understanding of the physiology of solitary bladder-wall-associated bacteria could contribute to the development of new strategies to eliminate persistent bladder infections.

STAR★METHODS

Detailed methods are provided in the online version of this paper and include the following:

- KEY RESOURCES TABLE
- RESOURCE AVAILABILITY
  - Lead contact
  - Materials availability
  - Data and code availability
- EXPERIMENTAL MODEL AND SUBJECT DETAILS
  - Mice
- METHOD DETAILS
  - Generation of mouse bladder organoids from mouse bladder uroepithelial cells
  - UPEC culture and injection of mouse bladder organoids
  - Isolation of neutrophils and labeling with CellTracker dye
  - Co-culture of mouse neutrophils and infected organoids in collagen gels
  - Quantitative real-time PCR (qRT-PCR) of infected organoid samples
  - Immunofluorescence of uninfected and infected mouse bladder organoids
  - Time-lapse confocal imaging of infected organoids
  - Ampicillin treatment of infected organoids
  - Image analysis for confocal live-cell imaging
  - Neutrophil spot detection
  - Serial block face-scanning electron microscopy (SBEM) of an infected organoid
  - Labeling of bacteria, epithelial cells, neutrophils, and organoid lumen in SBEM images
  - 3D analysis and modeling of the infected organoid
  - Scanning electron microscopy of infected organoids
- QUANTIFICATION AND STATISTICAL ANALYSIS

SUPPLEMENTAL INFORMATION

Supplemental information can be found online at https://doi.org/10.1016/j.celrep.2021.109351.

ACKNOWLEDGMENTS

V.V.T. acknowledges support by Long-Term Fellowships from the Human Frontier Science Program (HFSP; LT000231/2016-L) and the European Molecular Biology Organization (EMBO; 921-2015). This research was supported by grants to J.D.M. from the Swiss National Science Foundation (SNSF) (310030B_176397) and the National Centre of Competence in Research Anti-Resist funded by the SNSF (51NF40_180541). K.S. wishes to thank the members of the EPFL Bioimaging & Optics Core Facility for assistance in confocal live-cell imaging and analysis in Bitplane Imaris, D. Dutta and S. Rosset for help in optimizing the protocol for rupturing infected organoids, J. Sordet-Desimoz and G.-F. Mancini for assistance with paraffin-embedded slicing of organoids, G. Markus for development of the neutrophil isolation protocol, M. Nikolaev for assistance with the collagen gel polymerization protocol, T. Simonet for the UPEC Δ*fliC* strain, A. Marcos for optimizing the microinjection of bladder organoids, and A. Oates for access to a stereo microscope. The authors credit BioRender.com for the illustrations and schematics used in this manuscript.

AUTHOR CONTRIBUTIONS

Conceptualization: K.S., V.V.T., N.D., J.D.M.; methodology: K.S., V.V.T., N.D., G.K.,; software: K.S., V.V.T.; validation: K.S., V.V.T., N.D.; formal analysis: K.S., V.V.T., N.D.; investigation: K.S., V.V.T., N.D., F.S.-G., M.C.C., A.D., G.K.; resources: K.S., J.M., H.C.; data curation; K.S.; writing – original draft preparation: K.S., V.V.T.; writing – review and editing: K.S., V.V.T., N.D., F.S.-G., M.C.C., A.D., J.M., G.K., H.C., J.D.M.; visualization: K.S., V.V.T., N.D.; supervision: V.V.T., N.D., J.D.M.; project administration: K.S., V.V.T., N.D., J.D.M.; funding acquisition: J.D.M.

DECLARATION OF INTERESTS

The authors declare no competing interests.

Received: November 16, 2020
Revised: March 26, 2021
Accepted: June 15, 2021
Published: July 20, 2021

REFERENCES

Alteri, C.J., Smith, S.N., and Mobley, H.L.T. (2009). Fitness of Escherichia coli during urinary tract infection requires gluconeogenesis and the TCA cycle. PLoS Pathog. *5*, e1000448.

Andersen, T.E., Khandige, S., Madelung, M., Brewer, J., Kolmos, H.J., and Møller-Jensen, J. (2012). Escherichia coli uropathogenesis in vitro: invasion, cellular escape, and secondary infection analyzed in a human bladder cell infection model. Infect. Immun. *80*, 1858–1867.

Anderson, G.G., Palermo, J.J., Schilling, J.D., Roth, R., Heuser, J., and Hultgren, S.J. (2003). Intracellular bacterial biofilm-like pods in urinary tract infections. Science *301*, 105–107.

Anderson, G.G., Dodson, K.W., Hooton, T.M., and Hultgren, S.J. (2004). Intracellular bacterial communities of uropathogenic Escherichia coli in urinary tract pathogenesis. Trends Microbiol. *12*, 424–430.

Bartfeld, S., and Clevers, H. (2015). Organoids as Model for Infectious Diseases: Culture of Human and Murine Stomach Organoids and Microinjection of Helicobacter pylori. J. Vis. Exp. *12*, 53359.

Blango, M.G., and Mulvey, M.A. (2010). Persistence of uropathogenic Escherichia coli in the face of multiple antibiotics. Antimicrob. Agents Chemother. *54*, 1855–1863.

Blango, M.G., Ott, E.M., Erman, A., Veranic, P., and Mulvey, M.A. (2014). Forced resurgence and targeting of intracellular uropathogenic Escherichia coli reservoirs. PLoS One *9*, e93327.

Cattan, V., Bernard, G., Rousseau, A., Bouhout, S., Chabaud, S., Auger, F.A., and Bolduc, S. (2011). Mechanical stimuli-induced urothelial differentiation in a human tissue-engineered tubular genitourinary graft. Eur. Urol. *60*, 1291–1298.

Chabaud, S., Saba, I., Baratange, C., Boiroux, B., Leclerc, M., Rousseau, A., Bouhout, S., and Bolduc, S. (2017). Urothelial cell expansion and differentiation are improved by exposure to hypoxia. J. Tissue Eng. Regen. Med. *11*, 3090–3099.

Clevers, H. (2016). Modeling Development and Disease with Organoids. Cell *165*, 1586–1597.

Co, J.Y., Margalef-Català, M., Li, X., Mah, A.T., Kuo, C.J., Monack, D.M., and Amieva, M.R. (2019). Controlling Epithelial Polarity: A Human Enteroid Model for Host-Pathogen Interactions. Cell Rep. *26*, 2509–2520.e4.

Denk, W., and Horstmann, H. (2004). Serial block-face scanning electron microscopy to reconstruct three-dimensional tissue nanostructure. PLoS Biol. *2*, e329.

Epp, A., and Larochelle, A.Urogynaecology Committee; Family Physicians Advisory Committee (2010). Recurrent urinary tract infection. J. Obstet. Gynaecol. Can. *32*, 1082–1090.

Flores-Mireles, A.L., Walker, J.N., Caparon, M., and Hultgren, S.J. (2015). Urinary tract infections: epidemiology, mechanisms of infection and treatment options. Nat. Rev. Microbiol. *13*, 269–284.

Forsyth, V.S., Armbruster, C.E., Smith, S.N., Pirani, A., Springman, A.C., Walters, M.S., Nielubowicz, G.R., Himpsl, S.D., Snitkin, E.S., and Mobley, H.L.T. (2018). Rapid Growth of Uropathogenic *Escherichia coli* during Human Urinary Tract Infection. mBio *9*, e00186-e18.

Foxman, B. (2010). The epidemiology of urinary tract infection. Nat. Rev. Urol. *7*, 653–660.

Foxman, B., Gillespie, B., Koopman, J., Zhang, L., Palin, K., Tallman, P., Marsh, J.V., Spear, S., Sobel, J.D., Marty, M.J., and Marrs, C.F. (2000). Risk factors for second urinary tract infection among college women. Am. J. Epidemiol. *151*, 1194–1205.

Halstead, A.M., Kapadia, C.D., Bolzenius, J., Chu, C.E., Schriefer, A., Wartman, L.D., Bowman, G.R., and Arora, V.K. (2017). Bladder-cancer-associated mutations in *RXRA* activate peroxisome proliferator-activated receptors to drive urothelial proliferation. eLife *6*, e30862.

Hannan, T.J., and Hunstad, D.A. (2016). A Murine Model for Escherichia coli Urinary Tract Infection. Methods Mol. Biol. *1333*, 159–175.

Haraoka, M., Hang, L., Frendéus, B., Godaly, G., Burdick, M., Strieter, R., and Svanborg, C. (1999). Neutrophil recruitment and resistance to urinary tract infection. J. Infect. Dis. *180*, 1220–1229.

Heo, I., Dutta, D., Schaefer, D.A., Iakobachvili, N., Artegiani, B., Sachs, N., Boonekamp, K.E., Bowden, G., Hendrickx, A.P.A., Willems, R.J.L., et al. (2018). Modelling Cryptosporidium infection in human small intestinal and lung organoids. Nat. Microbiol. *3*, 814–823.

Hoffman, D.P., Shtengel, G., Xu, C.S., Campbell, K.R., Freeman, M., Wang, L., Milkie, D.E., Pasolli, H.A., Iyer, N., Bogovic, J.A., et al. (2020). Correlative three-dimensional super-resolution and block-face electron microscopy of whole vitreously frozen cells. Science *367*, eaaz5357.

Homan, K.A., Gupta, N., Kroll, K.T., Kolesky, D.B., Skylar-Scott, M., Miyoshi, T., Mau, D., Valerius, M.T., Ferrante, T., Bonventre, J.V., et al. (2019). Flow-enhanced vascularization and maturation of kidney organoids in vitro. Nat. Methods *16*, 255–262.

Hopke, A., Scherer, A., Kreuzburg, S., Abers, M.S., Zerbe, C.S., Dinauer, M.C., Mansour, M.K., and Irimia, D. (2020). Neutrophil swarming delays the growth of clusters of pathogenic fungi. Nat. Commun. *11*, 2031.

Horsley, H., Dharmasena, D., Malone-Lee, J., and Rohn, J.L. (2018). A urine-dependent human urothelial organoid offers a potential alternative to rodent models of infection. Sci. Rep. *8*, 1238.

Hull, R.A., and Hull, S.I. (1997). Nutritional requirements for growth of uropathogenic Escherichia coli in human urine. Infect. Immun. *65*, 1960–1961.

Hung, C.-S., Dodson, K.W., and Hultgren, S.J. (2009). A murine model of urinary tract infection. Nat. Protoc. *4*, 1230–1243.

Ingersoll, M.A., Kline, K.A., Nielsen, H.V., and Hultgren, S.J. (2008). G-CSF induction early in uropathogenic Escherichia coli infection of the urinary tract modulates host immunity. Cell. Microbiol. *10*, 2568–2578.

Isles, H.M., Loynes, C.A., Hamilton, N., Muir, C.F., Kadochnikova, A., Henry, K.M., Kadirkamanathan, V., Renshaw, S.A., and Elks, P.M. (2019). Endogenous pioneer neutrophils release NETs during the swarming response in zebrafish. biorxiv. https://doi.org/10.1101/521450.

Jorstad, A., Blanc, J., and Knott, G. (2018). NeuroMorph: A Software Toolset for 3D Analysis of Neurite Morphology and Connectivity. Front. Neuroanat. *12*, 59.

Justice, S.S., Hung, C., Theriot, J.A., Fletcher, D.A., Anderson, G.G., Footer, M.J., and Hultgren, S.J. (2004). Differentiation and developmental pathways of uropathogenic Escherichia coli in urinary tract pathogenesis. Proc. Natl. Acad. Sci. USA *101*, 1333–1338.

Justice, S.S., Hunstad, D.A., Seed, P.C., and Hultgren, S.J. (2006). Filamentation by Escherichia coli subverts innate defenses during urinary tract infection. Proc. Natl. Acad. Sci. USA *103*, 19884–19889.

Kessler, M., Hoffmann, K., Fritsche, K., Brinkmann, V., Mollenkopf, H.-J., Thieck, O., Teixeira da Costa, A.R., Braicu, E.I., Sehouli, J., Mangler, M., et al. (2019). Chronic Chlamydia infection in human organoids increases stemness and promotes age-dependent CpG methylation. Nat. Commun. *10*, 1194.

Kienle, K., and Lämmermann, T. (2016). Neutrophil swarming: an essential process of the neutrophil tissue response. Immunol. Rev. *273*, 76–93.

Kim, E., Choi, S., Kang, B., Kong, J., Kim, Y., Yoon, W.H., Lee, H.-R., Kim, S., Kim, H.-M., Lee, H., et al. (2020). Creation of bladder assembloids mimicking tissue regeneration and cancer. Nature *588*, 664–669.

Klein, R.D., and Hultgren, S.J. (2020). Urinary tract infections: microbial pathogenesis, host-pathogen interactions and new treatment strategies. Nat. Rev. Microbiol. *18*, 211–226.

Lacerda Mariano, L., Rousseau, M., Varet, H., Legendre, R., Gentek, R., Saenz Coronilla, J., Bajenoff, M., Gomez Perdiguero, E., and Ingersoll, M.A. (2020). Functionally distinct resident macrophage subsets differentially shape responses to infection in the bladder. Sci. Adv. *6*, eabc5739.

Lämmermann, T., Afonso, P.V., Angermann, B.R., Wang, J.M., Kastenmüller, W., Parent, C.A., and Germain, R.N. (2013). Neutrophil swarms require LTB4 and integrins at sites of cell death in vivo. Nature *498*, 371–375.

Lane, M.C., Alteri, C.J., Smith, S.N., and Mobley, H.L.T. (2007). Expression of flagella is coincident with uropathogenic Escherichia coli ascension to the upper urinary tract. Proc. Natl. Acad. Sci. USA *104*, 16669–16674.

Lee, S.H., Hu, W., Matulay, J.T., Silva, M.V., Owczarek, T.B., Kim, K., Chua, C.W., Barlow, L.J., Kandoth, C., Williams, A.B., et al. (2018). Tumor Evolution and Drug Response in Patient-Derived Organoid Models of Bladder Cancer. Cell *173*, 515–528.e17.

Lewis, A.J., Richards, A.C., and Mulvey, M.A. (2016). Invasion of Host Cells and Tissues by Uropathogenic Bacteria. Microbiol. Spectr. *4*. https://doi.org/10.1128/microbiolspec.UTI-0026-2016.

Liese, J., Rooijakkers, S.H.M., van Strijp, J.A.G., Novick, R.P., and Dustin, M.L. (2013). Intravital two-photon microscopy of host-pathogen interactions in a mouse model of Staphylococcus aureus skin abscess formation. Cell. Microbiol. *15*, 891–909.

Liu, Y., Stein, E., Oliver, T., Li, Y., Brunken, W.J., Koch, M., Tessier-Lavigne, M., and Hogan, B.L.M. (2004). Novel role for Netrins in regulating epithelial behavior during lung branching morphogenesis. Curr. Biol. *14*, 897–905.

Maclachlan, C., Sahlender, D.A., Hayashi, S., Molnár, Z., and Knott, G. (2018). Block Face Scanning Electron Microscopy of Fluorescently Labeled Axons Without Using Near Infra-Red Branding. Front. Neuroanat. *12*, 88.

Mansour, A.A., Gonçalves, J.T., Bloyd, C.W., Li, H., Fernandes, S., Quang, D., Johnston, S., Parylak, S.L., Jin, X., and Gage, F.H. (2018). An in vivo model of functional and vascularized human brain organoids. Nat. Biotechnol. *36*, 432–441.

Martinez, J.J., Mulvey, M.A., Schilling, J.D., Pinkner, J.S., and Hultgren, S.J. (2000). Type 1 pilus-mediated bacterial invasion of bladder epithelial cells. EMBO J. *19*, 2803–2812.

Mullenders, J., de Jongh, E., Brousali, A., Roosen, M., Blom, J.P.A., Begthel, H., Korving, J., Jonges, T., Kranenburg, O., Meijer, R., and Clevers, H.C. (2019). Mouse and human urothelial cancer organoids: A tool for bladder cancer research. Proc. Natl. Acad. Sci. USA *116*, 4567–4574.

Mulvey, M.A., Lopez-Boado, Y.S., Wilson, C.L., Roth, R., Parks, W.C., Heuser, J., and Hultgren, S.J. (1998). Induction and evasion of host defenses by type 1-piliated uropathogenic Escherichia coli. Science *282*, 1494–1497.

Mulvey, M.A., Schilling, J.D., Martinez, J.J., and Hultgren, S.J. (2000). Bad bugs and beleaguered bladders: interplay between uropathogenic Escherichia coli and innate host defenses. Proc. Natl. Acad. Sci. USA *97*, 8829–8835.

Mulvey, M.A., Schilling, J.D., and Hultgren, S.J. (2001). Establishment of a persistent Escherichia coli reservoir during the acute phase of a bladder infection. Infect. Immun. *69*, 4572–4579.

Muzumdar, M.D., Tasic, B., Miyamichi, K., Li, L., and Luo, L. (2007). A global double-fluorescent Cre reporter mouse. Genesis *45*, 593–605.

Mysorekar, I.U., and Hultgren, S.J. (2006). Mechanisms of uropathogenic Escherichia coli persistence and eradication from the urinary tract. Proc. Natl. Acad. Sci. USA *103*, 14170–14175.

Neal, J.T., Li, X., Zhu, J., Giangarra, V., Grzeskowiak, C.L., Ju, J., Liu, I.H., Chiou, S.-H., Salahudeen, A.A., Smith, A.R., et al. (2018). Organoid Modeling of the Tumor Immune Microenvironment. Cell *175*, 1972–1988.e16.

Nikolaev, M., Mitrofanova, O., Broguiere, N., Geraldo, S., Dutta, D., Tabata, Y., Elci, B., Brandenberg, N., Kolotuev, I., Gjorevski, N., et al. (2020). Homeostatic mini-intestines through scaffold-guided organoid morphogenesis. Nature *585*, 574–578.

Park, S.E., Georgescu, A., and Huh, D. (2019). Organoids-on-a-chip. Science *364*, 960–965.

Pleguezuelos-Manzano, C., Puschhof, J., Rosendahl Huber, A., van Hoeck, A., Wood, H.M., Nomburg, J., Gurjao, C., Manders, F., Dalmasso, G., Stege, P.B., et al.; Genomics England Research Consortium (2020). Mutational signature in colorectal cancer caused by genotoxic pks^{+} E. coli. Nature *580*, 269–273.

Poplimont, H., Georgantzoglou, A., Boulch, M., Walker, H.A., Coombs, C., Papaleonidopoulou, F., and Sarris, M. (2020). Neutrophil Swarming in Damaged Tissue Is Orchestrated by Connexins and Cooperative Calcium Alarm Signals. Curr. Biol. *30*, 2761–2776.e7.

Qian, X., Nguyen, H.N., Jacob, F., Song, H., and Ming, G.-L. (2017). Using brain organoids to understand Zika virus-induced microcephaly. Development *144*, 952–957.

Reátegui, E., Jalali, F., Khankhel, A.H., Wong, E., Cho, H., Lee, J., Serhan, C.N., Dalli, J., Elliott, H., and Irimia, D. (2017). Microscale arrays for the profiling of start and stop signals coordinating human-neutrophil swarming. Nat. Biomed. Eng. *1*, 0094.

Rossi, G., Manfrin, A., and Lutolf, M.P. (2018). Progress and potential in organoid research. Nat. Rev. Genet. *19*, 671–687.

Sachs, N., Papaspyropoulos, A., Zomer-van Ommen, D.D., Heo, I., Böttinger, L., Klay, D., Weeber, F., Huelsz-Prince, G., Iakobachvili, N., Amatngalim, G.D., et al. (2019). Long-term expanding human airway organoids for disease modeling. EMBO J. *38*, e100300.

Santos, C.P., Lapi, E., Martínez de Villarreal, J., Álvaro-Espinosa, L., Fernández-Barral, A., Barbáchano, A., Domínguez, O., Laughney, A.M., Megías, D., Muñoz, A., and Real, F.X. (2019). Urothelial organoids originating from Cd49f^{high} mouse stem cells display Notch-dependent differentiation capacity. Nat. Commun. *10*, 4407.

Schilling, J.D., Lorenz, R.G., and Hultgren, S.J. (2002). Effect of trimethoprim-sulfamethoxazole on recurrent bacteriuria and bacterial persistence in mice infected with uropathogenic Escherichia coli. Infect. Immun. *70*, 7042–7049.

Schiwon, M., Weisheit, C., Franken, L., Gutweiler, S., Dixit, A., Meyer-Schwesinger, C., Pohl, J.-M., Maurice, N.J., Thiebes, S., Lorenz, K., et al. (2014). Crosstalk between sentinel and helper macrophages permits neutrophil migration into infected uroepithelium. Cell *156*, 456–468.

Scott, V.C.S., Haake, D.A., Churchill, B.M., Justice, S.S., and Kim, J.-H. (2015). Intracellular Bacterial Communities: A Potential Etiology for Chronic Lower Urinary Tract Symptoms. Urology *86*, 425–431.

Semerad, C.L., Liu, F., Gregory, A.D., Stumpf, K., and Link, D.C. (2002). G-CSF is an essential regulator of neutrophil trafficking from the bone marrow to the blood. Immunity *17*, 413–423.

Shannon, J.G., Hasenkrug, A.M., Dorward, D.W., Nair, V., Carmody, A.B., and Hinnebusch, B.J. (2013). Yersinia pestis subverts the dermal neutrophil response in a mouse model of bubonic plague. MBio *4*, e00170-e13.

Sharma, K., Dhar, N., Thacker, V.V., Simonet, T.M., Signorino-Gelo, F., Knott, G.W., and McKinney, J.D. (2021). Dynamic persistence of UPEC intracellular bacterial communities in a human bladder-chip model of urinary tract infection. eLife *10*, e66481, In press. https://doi.org/10.7554/eLife.66481.

Shin, K., Lee, J., Guo, N., Kim, J., Lim, A., Qu, L., Mysorekar, I.U., and Beachy, P.A. (2011). Hedgehog/Wnt feedback supports regenerative proliferation of epithelial stem cells in bladder. Nature *472*, 110–114.

Smith, Y.C., Grande, K.K., Rasmussen, S.B., and O'Brien, A.D. (2006). Novel three-dimensional organoid model for evaluation of the interaction of uropathogenic Escherichia coli with terminally differentiated human urothelial cells. Infect. Immun. *74*, 750–757.

Southgate, J., Hutton, K.A., Thomas, D.F., and Trejdosiewicz, L.K. (1994). Normal human urothelial cells in vitro: proliferation and induction of stratification. Lab. Invest. *71*, 583–594.

Subashchandrabose, S., Hazen, T.H., Brumbaugh, A.R., Himpsl, S.D., Smith, S.N., Ernst, R.D., Rasko, D.A., and Mobley, H.L.T. (2014). Host-specific induction of Escherichia coli fitness genes during human urinary tract infection. Proc. Natl. Acad. Sci. USA *111*, 18327–18332.

Sundac, L., Dando, S.J., Sullivan, M.J., Derrington, P., Gerrard, J., and Ulett, G.C. (2016). Protein-based profiling of the immune response to uropathogenic Escherichia coli in adult patients immediately following hospital admission for acute cystitis. Pathog. Dis. *74*, ftw062.

Suzuki, K., Koyanagi-Aoi, M., Uehara, K., Hinata, N., Fujisawa, M., and Aoi, T. (2019). Directed differentiation of human induced pluripotent stem cells into mature stratified bladder urothelium. Sci. Rep. *9*, 10506.

Swamydas, M., Luo, Y., Dorf, M.E., and Lionakis, M.S. (2015). Isolation of Mouse Neutrophils. Curr. Protoc. Immunol. *110*, 3.20.1–3.20.15.

Takebe, T., Zhang, B., and Radisic, M. (2017). Synergistic Engineering: Organoids Meet Organs-on-a-Chip. Cell Stem Cell *21*, 297–300.

van der Sanden, S.M.G., Sachs, N., Koekkoek, S.M., Koen, G., Pajkrt, D., Clevers, H., and Wolthers, K.C. (2018). Enterovirus 71 infection of human airway organoids reveals VP1-145 as a viral infectivity determinant. Emerg. Microbes Infect. *7*, 84.

Wakamoto, Y., Dhar, N., Chait, R., Schneider, K., Signorino-Gelo, F., Leibler, S., and McKinney, J.D. (2013). Dynamic persistence of antibiotic-stressed mycobacteria. Science *339*, 91–95.

Williamson, I.A., Arnold, J.W., Samsa, L.A., Gaynor, L., DiSalvo, M., Cocchiaro, J.L., Carroll, I., Azcarate-Peril, M.A., Rawls, J.F., Allbritton, N.L., and Magness, S.T. (2018). A High-Throughput Organoid Microinjection Platform to Study Gastrointestinal Microbiota and Luminal Physiology. Cell. Mol. Gastroenterol. Hepatol. *6*, 301–319.

Wright, K.J., Seed, P.C., and Hultgren, S.J. (2005). Uropathogenic Escherichia coli flagella aid in efficient urinary tract colonization. Infect. Immun. *73*, 7657–7668.

Wright, K.J., Seed, P.C., and Hultgren, S.J. (2007). Development of intracellular bacterial communities of uropathogenic Escherichia coli depends on type 1 pili. Cell. Microbiol. *9*, 2230–2241.

Yu, L., O'Brien, V.P., Livny, J., Dorsey, D., Bandyopadhyay, N., Colonna, M., Caparon, M.G., Roberson, E.D., Hultgren, S.J., and Hannan, T.J. (2019). Mucosal infection rewires TNFα signaling dynamics to skew susceptibility to recurrence. eLife *8*, e46677.

Yuki, K., Cheng, N., Nakano, M., and Kuo, C.J. (2020). Organoid Models of Tumor Immunology. Trends Immunol. *41*, 652–664.

Zhang, B., Korolj, A., Lai, B.F.L., and Radisic, M. (2018). Advances in organ-on-a-chip engineering. Nat. Rev. Mater. *3*, 257–278.

Zhou, J., Li, C., Sachs, N., Chiu, M.C., Wong, B.H.-Y., Chu, H., Poon, V.K.-M., Wang, D., Zhao, X., Wen, L., et al. (2018). Differentiated human airway organoids to assess infectivity of emerging influenza virus. Proc. Natl. Acad. Sci. USA *115*, 6822–6827.

STAR★METHODS

KEY RESOURCES TABLE

REAGENT or RESOURCE	SOURCE	IDENTIFIER
Antibodies		
Anti-LPS	Abcam	Cat#: ab 35654; RRID:AB_732222
Anti-CK7	Abcam	Cat#: ab 209599
Anti-CK8	Abcam	Cat#: ab 192468; RRID:AB_2890258
Anti-CK13	Abcam	Cat#: ab 198584
Anti-Ly6G -PE	Biolegend	Cat#: 127607; RRID:AB_1186104
Anti-CD11b -BV711	Biolegend	Cat#: 101241; RRID:AB_11218791
Anti-flagellin	Abcam	Cat#: ab 93713; RRID:AB_10563522
Anti-p63	Abcam	Cat#: ab 735; RRID:AB_305870
Anti-Uroplakin3a	Santa Cruz	Cat#: sc-166808; RRID:AB_2241422
Donkey anti-Mouse IgG (H+L) Highly Cross-Adsorbed Secondary Antibody, Alexa Fluor 647	Thermofisher	Cat#: A-31571; RRID:AB_162542
Donkey anti-Rabbit IgG (H+L) Highly Cross-Adsorbed Secondary Antibody, Alexa Fluor 647	Thermofisher	Cat#: A-31573; RRID:AB_2536183
Goat anti-Mouse IgG (H+L) Highly Cross-Adsorbed Secondary Antibody, Alexa Fluor 488	Thermofisher	Cat#: A-11029; RRID:AB_138404
Bacterial and virus strains		
Uropathogenic *Escherichia coli* (UPEC) strain CFT073	PMID: 2182540	NCBI:txid199310
CFT073-pZA32-YFP	This paper	N/A
Chemicals, peptides, and recombinant proteins		
Native Collagen, Bovine dermis	AteloCell	Cat#: IAC-50
B27	Thermofisher	Cat#:17504044
Human KGF/ FGF7	Peprotech	Cat#:100-19
Human FGF10	Peprotech	Cat#:100-26
Cultrex PathClear Reduced Growth Factor BME, Type 2	Bio-Techne	Cat#: 3533-005-02
Ampicillin	Sigma-Aldrich	Cat#: A9518-5G
Chloramphenicol	Sigma-Aldrich	Cat#:C1919-25G
GIBCO Trypsin-EDTA (0.05%), phenol red	Thermofisher	Cat#:25300054
GIBCO Antibiotic-Antimycotic (100X)	Thermofisher	Cat#:15240062
GIBCO Fetal Bovine Serum	Thermofisher	Cat#: 10270106
GIBCO RPMI 1640 Medium, no phenol red	Thermofisher	Cat#:11835030
RPMI-1640 medium	ATCC	Cat#:30-2001
Critical commercial assays		
Anti-Ly-6G MicroBead Kit, mouse	Miltenyi Biotec	Cat#: 130-092-332
Deposited data		
Data generated in this study	Zenodo	https://doi.org/10.5281/zenodo.4772818
Experimental models: Organisms/strains		
Gt(ROSA)26Sortm4(ACTB-tdTomato,-EGFP)Luo/J	Jackson Laboratory	Cat#: 007576; RRID:IMSR_JAX:007576; PMID: 17868096
C57BL/6 Mouse	Charles River Laboratory	Cat#: C57BL/6NCrl
Oligonucleotides		
GGT GCC TAT GTC TCA GCC TCT T	Microsynth	*Tnfa* forward
GCC ATA GAA CTG ATG AGA GGG AG	Microsynth	*Tnfa* reverse

(*Continued on next page*)

CellPress
OPEN ACCESS

Continued

REAGENT or RESOURCE	SOURCE	IDENTIFIER
CAT CCA GAG CTT GAG TGT GAC G	Microsynth	*Cxcl2* forward
GGC TTC AGG GTC AAG GCA AAC T	Microsynth	*Cxcl2* reverse
TAC CAC TTC ACA AGT CGG AGG C	Microsynth	*Il6* forward
CTG CAA GTG CAT CAT CGT TGT TC	Microsynth	*Il6* reverse
TGG ACC TTC CAG GAT GAG GAC A	Microsynth	*Il1b* forward
GTT CAT CTC GGA GCC TGT AGT G	Microsynth	*Il1b* reverse
GCT ACA AGA GGA TCA CCA GCA G	Microsynth	*Ccl2* forward
GTC TGG ACC CAT TCC TTC TTG G	Microsynth	*Ccl2* reverse
ACT GCC TGC TGC TTC TCC TAC A	Microsynth	*Ccl3* forward
ATG ACA CCT GGC TGG GAG CAA A	Microsynth	*Ccl3* reverse
ACC CTC CCA CTT CCT GCT GTT T	Microsynth	*Ccl4* forward
CTG TCT GCC TCT TTT GGT CAG G	Microsynth	*Ccl4* reverse
CGG GAA GAC AAT AAC TGC ACC C	Microsynth	*Il10* forward
CGG TTA GCA GTA TGT TGT CCA GC	Microsynth	*Il10* reverse
Recombinant DNA		
pZA32-YFP	PMID: 9092630	N/A
Software and algorithms		
Imaris 9.5.1	Bitplane	RRID:SCR_007370; https://imaris.oxinst.com/
Prism	Graphpad	RRID:SCR_002798; https://www.graphpad.com/
Other		
Advanced DMEM/F-12	Thermofisher	Cat#: 12634010
DMEM/F-12, no phenol red	Thermofisher	Cat#: 21041025
HEPES, 100X	Thermofisher	Cat#:15630106
Glutamax, 100X	Thermofisher	Cat#: 35050061
A8301	Tocris	Cat#: 2939
Rho kinase inhibitor, Y-27632	Abmole Bioscience	Cat#: 2939
Glass Pasteur pipettes	VWR	Cat#: 612-1701
Gas chamber for stages with k-frame insert (160x110mm) - magnetic model with sliding lid.	Okolab	Cat#: H201-K-FRAME
Flaming/Brown Micropipette Puller	Sutter Instruments	model P-87
Capillary glass, 1.0 mm outer diameter, 0.75 mm inner diameter	WPI	TW100F-4
35mm holder - magnetic	Okolab	Cat#:1x35-M
μ-Dish 35 mm, high	Ibidi	Cat#:81156
Flexible tubing, 0.76X1.65X0.45X15000	Freudenberg Medical	Cat#:0045634143
1.00/0.75 × 20mm metallic tubes	Unimed	Cat#:200.010-A
Aladdin programmable pump	WPI	Cat#:PUMP-NE-1000
Olympus SZX16 stereo microscope	Olympus	N/A
Leica SP8 confocal microscope	Leica	N/A
Olympus MVX10 stereo microscope	Olympus	RRID:SCR_018612
CellTracker Deep Red Dye	Thermofisher	Cat#: C34565
LB (Luria broth base, Miller's modified)	Sigma-Aldrich	Cat#: L1900-1KG
Invitrogen DAPI	Thermofisher	Cat#: D1306
TrypLE Express Enzyme (1X)	Thermofisher	Cat#: 12605010
Phosphate Buffered Saline	Thermofisher	Cat#: 10010056
Lucifer Yellow CH, Lithium Salt	Thermofisher	Cat#: L453
pHrodo Deep Red *E. coli* BioParticles Conjugate for Phagocytosis	Thermofisher	Cat#: P35360

RESOURCE AVAILABILITY

Lead contact

Further information and requests for resources and reagents should be directed to and will be fulfilled by the Lead Contact, John D. McKinney (john.mckinney@epfl.ch).

Materials availability

All unique/stable reagents generated in this study are available from the Lead Contact with a completed Materials Transfer Agreement.

Data and code availability

The datasets/code generated during this study are available at Zenodo, https://doi.org/10.5281/zenodo.4772818.

EXPERIMENTAL MODEL AND SUBJECT DETAILS

Mice

Female C57BL/6 mice (Charles River Laboratories) aged 2-4 months or female ROSA$^{MT/MG}$ mice (Jackson Laboratories) at age 4 months. Mice used for these experiments were housed in a specific pathogen-free facility. All animal protocols were reviewed and approved by EPFL's Chief Veterinarian, by the Service de la Consommation et des Affaires Vétérinaires of the Canton of Vaud, and by the Swiss Office Vétérinaire Fédéral.

METHOD DETAILS

Generation of mouse bladder organoids from mouse bladder uroepithelial cells

C57BL/6 mice (Charles River Laboratories) and ROSA$^{MT/MG}$ mice (Jackson Laboratories) were housed in a specific pathogen-free facility. Mouse bladder organoids were prepared by selectively isolating bladder lumenal cells following the procedure described in Mullenders et al. (2019). For the generation of large numbers of organoids, three female mice at age four months were euthanized by CO_2 overdose. Lumenal uroepithelial cells were isolated by microinjecting ~500 μL TryPLE (GIBCO) with a 26-gauge needle (Terumo) into the bladder lumen. During this procedure, the urinary bladder was clamped at the outlet. Subsequently, the clamped urinary bladder, filled with TrypLE solution, was immersed in 20 mL pre-warmed Basal Medium (Advanced DMEM/F-12 medium) and placed in a 50 mL Falcon tube. The Falcon tube containing the bladder was subsequently incubated for 1 hour in a cell culture incubator maintained at 37°C and 5% CO_2. The lumen of the bladder was then washed twice with basal medium containing 20% heat-inactivated fetal bovine serum (FBS, GIBCO) to neutralize the effect of TryPLE. The cell suspension was passed through a 40 μm filter (Fisher) and the cells in the flow-through were centrifuged at 300 g for 5 minutes. These isolated uroepithelial cells were then resuspended in an appropriate volume of Cultrex Basement Membrane Extract (BME) and seeded as hemispherical domes (40-50 μl) in individual wells of a 24-well plate (BD Falcon). The 24-well plate was placed in a cell culture incubator for 30 minutes in an inverted configuration to promote 3D growth. The solidified hemispherical domes were then surrounded by mouse bladder medium (MBM) (Mullenders et al., 2019) supplemented with 1X antibacterial/antifungal solution (GIBCO). MBM medium consists of Advanced DMEM/F-12 medium (Thermofisher), 100 ng/ml of FGF10 (Peprotech), 25 ng/ml of FGF7 (Peprotech), 500 nM of A83-01 (Tocris Bioscience), 2% of B27 (Thermofisher), and 10 μM of Y-27632 ROCK inhibitor (Abmole Bioscience). Over the subsequent 2-3 weeks, the mouse bladder organoids were either passaged every 5 days or sheared with a fire-polished glass pipette to reduce the size of the organoids. Thereafter, the organoids were used immediately or cryopreserved in freezing medium (60% FBS, 30% Advanced DMEM/F-12, 10% DMSO) at −180°C for subsequent experiments.

UPEC culture and injection of mouse bladder organoids

Uropathogenic *Escherichia coli* (UPEC) strain CFT073 was isolated from a patient with pyelonephritis and provided by H.L.T. Mobley. A derivative strain expressing yellow fluorescent protein (YFP) was generated by electroporation of CFT073 with the episomal plasmid PZA32-YFP. To induce expression of type 1 pili, UPEC was grown in LB media containing 25 μg/ml chloramphenicol in non-shaking condition at 37°C for 2 days prior to the experiment. Cryopreserved tdTomato mouse bladder organoids were thawed and recultured in BME for five days before the experiment. On the day prior to the experiment, the organoids were washed twice with ice-cold DMEM (without antibacterials or antifungals) followed by centrifugation at 100 g for 5 minutes to remove the spent BME. They were then seeded in fresh BME inside a 35 mm ibidi μ-Dish in basal medium without antibacterial or antifungal supplementation. On the day of the experiment, stationary-phase UPEC were microinjected into the organoid lumen using a Pneumatic PicoPump (WPI). The micropipettes used for microinjection were prepared from thin wall glass capillary (TW100F-4 with length 100 mm and diameter 1 mm) using a Flaming/Brown Micropipette Puller (Sutter Instruments model P-87) set at pressure 360, heat 866, Vel 200. Prior to microinjection, the micropipettes were filled with 10 μl of 1:1 dilution of UPEC culture with a Phenol Red solution (Sigma-Aldrich) using Microloader flexible tips (Eppendorf) to facilitate the visualization of the injected volume. The micropipettes were then cut with a sharp scalpel under a stereomicroscope (Olympus SZX-16) to generate a wider tip. The tip size of the cut

micropipette was verified by setting pressure conditions adjusting the input pressure on PicoPump to eject ca. 1 nL volume of liquid in mineral oil on a thin film of paraffin on a Zeiss coverslide (corresponding to 100 μm). We verified the inoculum size by plating for colony-forming units (CFU) on LB agar. The mean inoculum for three separate experiments was 904 ± 340 CFU, 798 ± 199 CFU, and 413 ± 9 CFU respectively obtained from five technical replicates in each case. Typically, we aimed to inject medium-sized organoids (100-300 μm in diameter) with a clearly distinguishable lumen, as these were not only the easiest organoids to inject but were also of a size that was amenable to whole organoid live-cell imaging.

For experiments in which infected organoids were co-cultured with mouse bone marrow-derived neutrophils, the injected organoids were removed from fresh BME by pipetting 2 mL of ice-cold Cell Recovery Solution (Corning) after removing MBM from the ibidi μ-Dish. The BME hydrogel was mechanically dissociated with a P1000 pipette and the resulting liquid gel was placed inside a 15 mL Falcon tube pre-coated with a 1% BSA solution. The ibidi μ-Dish was washed twice with an additional 1.5 mL of Cell Recovery Solution to collect the organoids, and the resulting 5 mL of Cell Recovery Solution containing organoids inside the 15 mL Falcon tube was further mechanically dissociated with a non-tapered glass pipette pre-coated with a 1% BSA solution to ensure the complete removal of the organoids from the BME hydrogel. The cell recovery solution containing infected organoids was kept on ice for 30 minutes to completely liquefy the BME. The cell recovery solution was then exchanged through two washes with 10 mL of basal medium (supplemented with 10% FBS) and the organoids were centrifuged at 100 g for 5 minutes at 4°C to remove the recovery solution. The organoid pellet was then resuspended in a collagen gel that was suitable to observe the migratory dynamics of the neutrophils.

Isolation of neutrophils and labeling with CellTracker dye

For each experiment, neutrophils were isolated from bone marrow of three female WT mice aged between 2 and 4 months (Charles River). Briefly, mice were euthanized by CO_2 overdose and the femur and tibia were isolated. The isolated bone marrow was crushed with a mortar and pestle and resuspended in 5 mL of cold SM++ solution (HBSS + 2% serum + 25 mM HEPES). The tissue homogenate was then passed through a pre-wet 40 μm filter. An additional volume of cold SM++ solution was added to the filtered cell suspension to make a total volume of 50 mL and then pelleted at 300 g for 5 minutes. The cell suspension was processed in batches of 10^7 cells and neutrophils were isolated using positive selection with the Miltenyi Anti-Ly6G kit following the manufacturer's protocol (Swamydas et al., 2015). Isolated Ly6G mice neutrophils were stained with 1 μM CellTracker Deep Red (Thermofisher) in RPMI medium free of serum and phenol red and incubated for 30 minutes in 5 mL of cell suspension in a 50 mL Falcon tube maintained at 37°C. Neutrophils were labeled with Post-CellTracker then washed twice with 10 mL of 20% FBS in RPMI medium free of phenol red to remove the unbound dye. The labeled neutrophils were kept briefly at room temperature before introduction into a co-culture with infected organoids inside the collagen gel.

Co-culture of mouse neutrophils and infected organoids in collagen gels

Collagen gels were used to co-culture infected organoids and mouse neutrophils. The collagen gel master mix buffered at pH 7.0 was made by adding 312 μl of ice-cold native bovine collagen with 4 μl of 1 M HEPES, 4 μl of 1 M sodium bicarbonate, 40 μl of 1X DMEM/F-12, and 40 μl of 10X DMEM/F-12. The collagen gel mixture was stored on ice before use and care was taken to avoid generating bubbles when pipetting. Freshly isolated neutrophils (ca. 10^7 cells) labeled with CellTracker were resuspended in 88 μl of a premade mixture of collagen gel master mix (10X DMEM/F-12, 1X DMEM/F-12, HEPES, sodium bicarbonate) without native bovine collagen on ice and then mixed with infected organoids. 156 μl of collagen solution was added twice to the suspension of infected organoids and neutrophils on ice followed by rapid mixing with a P200 pipette. This collagen gel suspension of infected organoids and neutrophils was pipetted onto the surface of an ibidi μ-Dish, which was pretreated with plasma (Diener, pressure 60 for 60 s) to increase the hydrophilicity of the surface. This enabled a uniform thin layer (1-2 mm) of collagen gel to be deposited on the dish, which was required for imaging with a confocal microscope. The collagen gel was then incubated at 37°C and 5% CO_2 for 30 minutes to allow the collagen gel to polymerize and solidify. Lastly, 1.5 mL of a 25 ng/ml solution of murine Granulocyte Colony Stimulating Factor (G-CSF) was added to the co-culture of infected organoids and neutrophils to ensure that the neutrophils were exposed to chemokines that stimulate maturation (Ingersoll et al., 2008; Semerad et al., 2002).

Quantitative real-time PCR (qRT-PCR) of infected organoid samples

Organoids were infected as described above and four hours after microinjection of UPEC the cell culture media surrounding the organoids was removed, the organoids were incubated with the appropriate volume of RNA lysis buffer (RNAeasy Plus Micro Kit, QIAGEN), and RNA was isolated following the manufacturer's instructions and resuspended in 14 μL of DEPC-treated water. A similar procedure was followed for uninfected control organoids. 11 μL of the RNA-containing solution was used to generate cDNA using the SuperScriptIV First-Strand Synthesis System with random hexamers (Invitrogen), which was stored at –20°C. qRT-PCR primer sequences are listed in the Key resources table. qRT-PCR reactions were prepared with SYBRGreen PCR Master Mix (Applied Biosystems) with 500 nM primers, and 1 μL cDNA. Reactions were run for absolute quantification on an ABI PRISM7900HT Sequence Detection System (Applied Biosystems) and amplicon specificity was confirmed by melting-curve analysis.

Immunofluorescence of uninfected and infected mouse bladder organoids

For immunofluorescence imaging of paraffin-embedded slices, cryopreserved mouse bladder organoids were thawed and maintained in BME culture for five days before use. Both uninfected and infected organoids were fixed with 4% paraformaldehyde

(PFA) for 6 hours at room temperature with occasional mechanical dissociation with a P1000 pipette. Fixed organoids were then washed twice with PBS and centrifuged at 100 g for 5 minutes in a 15 mL Falcon tube pre-coated with 1% BSA. The organoids were resuspended in 50 μl of prewarmed Histogel (Thermofisher) at 50°C and pipetted out as a small hemispherical dome inside a 1-cm Tissue-Tek Cryomold. The cryomold was placed on a cold ice plate for solidification. Subsequently, the hemispherical Histogel was processed for paraffin embedding. Organoids embedded in paraffin were cut into 4 μm slices. The thin paraffin sections were deparaffinized and rehydrated by immersing the slides through the following solutions: xylene, three washes of 5 minutes each; 100% ethanol, two washes of 10 minutes each; 95% ethanol, two washes of 10 minutes each; 70% ethanol, two washes of 10 minutes each; 50% ethanol, two washes of 10 minutes each; PBS, three washes of 5 minutes each. Rehydrated slides were then processed for heat-induced antigen retrieval using 10 mM citrate buffer (pH 6.0). Slides were washed with 1X PBS, permeabilized with 0.15% Triton X-100 for 15 minutes, washed twice with 1X PBS, and blocked with 1% BSA in PBS for 1 hour. The boundaries of paraffin sections were marked with a hydrophobic pen and slides were labeled with a permanent ethanol-resistant marker. Incubation with primary antibodies at a dilution of 10 μg/ml or 1:100 was performed overnight in an antibody incubation buffer comprising 1% BSA and 0.01% Triton X-100 in PBS. Slides were subsequently washed three times with PBS for 10 minutes per wash. Incubation with secondary antibodies was performed at 2 μg/ml in antibody incubation buffer for 1 hour at room temperature. In each step, excess antibody was removed by washing three times with PBS for 10 minutes per wash. Cell nuclei were stained with DAPI (5 μg/ml, Thermofisher) for 30 minutes and slides were mounted with Fluoromount-G mounting medium (Thermofisher) overnight in a dark chamber. For immunofluorescence imaging of whole organoids, uninfected and infected organoids were cultured for 6 hours in collagen gels on ibidi μ-Dishes, fixed with 1 mL of 4% PFA for 1 hour, and antibody labeling was performed as described above.

Time-lapse confocal imaging of infected organoids

Imaging experiments were conducted using a Leica SP8 confocal microscope in the inverted configuration with a temperature-controlled microscope environmental chamber maintained at 37°C and 5% CO_2 in a stage-top chamber (OKOlabs). Time-lapse imaging was conducted using a Leica HC FLUOTAR 25X (NA 0.95) multi-immersion objective. To maintain the water immersion for the objective, water was pumped to the ring around the water objective at 9 Hz with pumping duration 10 s and pumping interval 30 minutes, controlled by SRS software. Microinjected tdTomato-expressing organoids were identified and imaged on either two channels (for experiments without neutrophils) or three channels (for experiments with neutrophils); in each case, multiple channels were acquired during the same imaging sequence to improve the temporal resolution. We used laser excitation wavelengths of 500 nm (YFP), 555 nm (tdTomato), and 630 nm (CellTracker Deep Red) to enable multi-channel imaging within the same sequence with reduced spectral overlap. Images were acquired with a scan speed of 700 Hz and a zoom factor of 2.25, which provided an XY resolution of 200-450 nm, corresponding to images of 1024 × 1024 pixels or 512 × 512 pixels, respectively. Z stacks were acquired with 0.5 or 1 μm step sizes.

Ampicillin treatment of infected organoids

After UPEC microinjection, MBOs were resuspended in collagen and supplemented with 1.5 mL of MBM medium following collagen polymerization for 30 minutes. Prior to the experiment, ibidi μ-Dishes were modified by inserting bent metallic tubes (1.00/0.75 × 20mm, Unimed Catalogue 200.010-A) through the lid and sealing these devices with PDMS cured in an oven at 80°C for 1 hour. Flexible 0.76 mm x 1.65 mm x 1 mm tubing (Mono-Lumen Freudenberg Medical) was connected to these tubes to facilitate medium addition and removal. A setup period of 2 to 3 hours was typically required and is not considered within the time duration of the experiment. Once imaging commenced, bacteria were allowed to grow for a 3-hour "growth phase" (0-165 minutes). The medium in the μ-Dish was then replaced with fresh medium containing ampicillin at 64.5 μg/ml, corresponding to 10X MIC. The dynamics of bacterial growth and killing in the presence of ampicillin was then monitored for a 3-hour "treatment phase" (ca. 165-345 minutes), after which ampicillin was removed from the extracellular medium by gentle exchange with fresh MBM media using a 20 mL syringe. Bacterial growth after ampicillin washout was monitored for a further 3-hour "regrowth phase" (345-525 minutes). Focus drift was adjusted manually at frequent intervals throughout the experiment.

For experiments to test the kinetics of ampicillin diffusion into the organoids, organoids were microinjected with pHrodo Deep Red *E. coli* BioParticles diluted ten times in LB to mimic microinjection with UPEC. The injected organoids were then resuspended in collagen in the μ-Dish as described previously. Organoids injected with pHrodo particle and uninjected bystander organoids were imaged for a period of 45 minutes with an imaging period of 15 minutes. Thereafter, we administered lucifer yellow (Thermofisher, 0.2 μM reconstituted in a 0.1 M solution of Tris buffer at pH 7.4) along with ampicillin (64.5 μg/ml) in MBM medium. The medium containing lucifer yellow and ampicillin was removed from the extracellular medium at the end of the 3-hour treatment period by gentle exchange with fresh MBM media using a 20 mL syringe. The mean intensity of lucifer yellow was computed within injected and bystander organoids by creating intraorganoid mask using tdTomato fluorescence of the epithelial cells as described in the section below. Mean lucifer yellow intensity in the extraorganoid environment was calculated within a bounding box (20 × 20 × 33 μm^3) located within an appropriate volume outside the organoid.

Image analysis for confocal live-cell imaging

Image analysis was performed with Bitplane Imaris 9.5.1. as outlined in greater detail in Figure S2 (for the analyses related to Figures 2 and S1) and Figure S4 (for the analyses related to Figures 4, 5, and S5). The following is a step-by-step summary of the analysis

pipeline as applied for the analysis in Figures 4 and 5. The time-lapse images acquired have four optical channels for UPEC (first channel), uroepithelial cells (second channel), neutrophils (third channel), and transmitted light (fourth channel). First, a background subtraction for the neutrophil channel was performed due to spectral overlap between the tdTomato expression from the epithelial cells and the CellTracker Deep Red staining of the neutrophils. This procedure allowed for a more robust detection of neutrophils inside the organoids. This created a fifth channel (Figure S4B). Next the organoid surfaces were generated using the Surface Generation Tool as outlined in Figure S4C. When required, adjacent bystander organoids were separated by setting the expected volume of the organoids using the seed point diameter function to automatically segment the organoids (depending upon the size of nearby organoids). In some cases, adjoining organoid surfaces were orthogonally trimmed with the cut tool. The organoid surface was then used as a mask to spatially distinguish intraorganoid versus extraorganoid bacterial and neutrophil populations (Figures S4D and S4E). These were stored as separate imaging channels in Imaris. Lastly, the intraorganoid and extraorganoid neutrophil channels were segmented to generated structures whose surfaces are depicted in the processed images in Figures 4A–4C, 5A–5C, and S5D–S5F and whose volumes are quantified in Figures 4D–4F, S5A–S5C, and S5G–S5L. In a similar fashion, intraorganoid UPEC was segmented to generate structures whose surfaces are shown in Figures 2B–2I and S1A and whose volumes were used to calculate the intraoorganoid bacterial growth kinetics in Figures 2J–2M and S1C and total bacterial volume inside the organoid in Figures 5D, S5A–S5C, and S5J–S5L.

Neutrophil spot detection

The masked sixth channel was also used to detect neutrophil spots (Size, 8 μm; Quality, 4 to 8) inside the organoid. Neutrophil spots in the field of view were detected on the neutrophil channel (third channel) with parameters (Size, 8 μm; Quality, 4 to 8). Neither neutrophil spots nor neutrophil surfaces were tracked over time due to the technical difficulties with imaging speed and amorphous shapes of migrating neutrophils around infected organoids. Average neutrophil sphericity ($\geq$0.5) for neutrophils around an organoid was obtained with time-collapsed information of average neutrophil sphericity for all the neutrophil surfaces per time point. In cases of larger neutrophil clusters, average neutrophil sphericity was obtained by excluding sphericity of the larger neutrophil cluster (< 0.5).

Serial block face-scanning electron microscopy (SBEM) of an infected organoid

Organoids expressing tdTomato were grown in ibidi μ-Dishes and microinjected with UPEC, which was allowed to grow within the organoid lumen for six hours. After two hours of bacterial growth, injected organoids were removed from fresh BME and resuspended in collagen gel surrounded by isolated bone marrow-derived neutrophils, as described above. The organoids were then plated in MBM supplemented with 25 ng/ml of mouse G-CSF on a plasma-treated MatTek dish with a gridded coverslip that enabled correlated light and electron microscopy. After 6 hours, organoids were fixed for 1 hour at room temperature in a 15 mL Falcon tube containing a mix of 1% glutaraldehyde and 2% paraformaldehyde in 0.1 M phosphate buffer (pH 7.4). Infected organoids were fixed for one hour then washed twice with PBS. The organoids were screened using optical microscopy to rapidly identify infected organoids with at least one IBC and neutrophils within the lumen suitable for volumetric electron microscopy. The selected organoid was imaged on the Leica SO8 microscope using a 10X objective to acquire a fluorescence image, which was used to identify and locate the target organoid on the gridded coverslip for correlated optical microscopy and SBEM. The fixed organoids were kept overnight at 4°C in the fixative, then postfixed in potassium ferrocyanide (1.5%) and osmium (2%) and stained with thiocarbohydrazide (1%) followed by osmium tetroxide (2%) alone. The organoids were finally stained overnight in uranyl acetate (1%) and washed in distilled water at 50°C before staining with lead aspartate (pH 5.5) at the same temperature. The entire coverslip, with the organoids attached, was dehydrated in increasing concentrations of alcohol and then embedded in durcupan resin and hardened at 65°C for 24 hours. The total thickness of the coverslip and resin was minimized to around 1 mm. Once hardened, the coverslip was removed and the region of resin containing the organoid of interest was cut away from the others with a scalpel blade. This piece was glued with conductive glue to an aluminum holder, then placed inside the scanning electron microscope (Merlin, Zeiss NTS) integrated with an in-chamber ultramicrotome device (3View, Gatan). Image of serial slices, 100 nm part, were collected from the block face using a beam energy of 1.7 kV and 350 pA of current. Each image contained 6144 × 4608 pixels with a pixel size of 30 nm. The stack contained 960 serial images. The overall volume imaged was 184.32 × 138.24 × 96 μm^3.

Labeling of bacteria, epithelial cells, neutrophils, and organoid lumen in SBEM images

Identification and labeling of different features (e.g., lumen boundary, neutrophils, bacteria) was done manually; features whose identity was doubtful were not included in the analysis. All of the different bacterial categories were identified on each slice of the full stack (960 slices). We identified five different categories of bacteria based on their location: extracellular bacteria in the organoid lumen, bacteria within neutrophils, bacteria within an IBC, bacteria within the cytoplasm of an uroepithelial cell, and pericellular bacteria sandwiched between the boundaries of adjacent cells. The injection site could be identified by the asymmetric distribution of lumenal bacteria with a higher abundance of extracellular lumenal bacteria toward one side of the lumen. We used the high fluorescence intensity of the large number of bacteria within the IBC to register and align the fluorescent image with the SBEM stack. In order to delineate structural features of the organoid, such as the boundary of the organoid lumen and the boundaries of the neutrophils as well as the overall organoid volume, a reduced stack (480 slices) with X, Y, Z pixel resolution of 60 nm, 60 nm, and 100 nm was generated. We also used this reduced stack to mark the location of all the uroepithelial cell nuclei within the organoid. Neutrophils were identified in electron microscope images based on their multi-lobular nuclei and high electron density; in ambiguous cases, the

fluorescent images of neutrophils labeled with CellTracker Deep Red were used to verify neutrophil identity. Altogether we identified five neutrophils surrounding the organoid and nine neutrophils inside the organoid.

3D analysis and modeling of the infected organoid

Serial electron micrographs were imported into the TrakEM2 plugin in FIJI. They were then aligned and registered and the locations of all cells and bacteria were annotated manually through the image stack. The organoid lumen was demarcated by segmenting the lumen boundary in each of the slices of the stack in each of the images in which it appeared. A similar procedure was used to define the boundaries of the neutrophils and the boundaries of the cells surrounding the IBC and containing the IBC. For ease of manipulating the large dataset, reconstructions of the lumen and identification of neutrophils and uroepithelial cells was done on a reduced stack of 480 slices with corresponding pixel size of 60 nm and spacing between serial slices of 200 nm. The segmentations of cells and the organoid lumen, and the coordinates of each mouse cell and bacterial cell, were then exported as a 3D wavefront object in TrakEM2 and imported into the Blender 3D modeling software. The proximity tool in the NeuroMorph toolset for Blender (Jorstad et al., 2018) was used to measure the distance of each bacterium to the wall of the lumen, as well as the organoid's external surface. To visualize the organoid, with all bacteria, the particles system in the Blender software was used to place a single generic model of either a bacterium or a cell at the vertex that marked its 3D coordinate.

Scanning electron microscopy of infected organoids

tdTomato-expressing organoids were infected with UPEC and incubated at 37°C for 6 hours. After this period the organoids were fixed for 1 hour at room temperature in a 15 mL Falcon tube containing a mix of 1% glutaraldehyde and 2% paraformaldehyde in 0.1 M phosphate buffer (pH 7.4). Fixed organoids were then seeded onto 12 mm poly-L-lysine-coated coverslips and stored overnight in the fixative. The organoids were further fixed with 1% osmium tetroxide in 0.1 M cacodylate buffer, followed by a dehydration step in increasing concentrations of ethanol (50% to 100% in 10% increments, 10 minutes per incubation). The dehydrated organoids were then dried at the critical point of CO_2 (Leica CPD300) before being ruptured with a 0.125 mm tungsten needle (FST, 10130-05) using a stereomicroscope (Leica M205). The ruptured organoid was then adhered to the surface of an aluminum stub using conductive tape (Election Microscopy Sciences, USA). This holder was coated with a 5-nm-thick layer of gold palladium metal using a Q150 sputter coater (Quorum Ltd, UK), then imaged in a scanning electron microscope (Merlin, Zeiss NTS). Images were acquired with an electron beam voltage of 1.50 kV and current of 80 pA with an HE-SE2 detector.

QUANTIFICATION AND STATISTICAL ANALYSIS

All statistical analysis was performed using Graphpad Prism. Details of the statistical tests and exact numbers of biological and technical replicates are provided in the figure legends, which also provide information about the depiction of the mean or median values and standard deviations or standard errors of the mean and confidence intervals where appropriate.